

# A Review on Metamaterial Application in Microstrip and Substrate Integrated Waveguide Antenna Designs

Wriddhi Bhowmik<sup>1, \*</sup>, Bhargav Appasani<sup>1</sup>, Amit K. Jha<sup>1</sup>, and Shweta Srivastava<sup>2</sup>

**Abstract**—Metamaterials are artificially configured composite materials exhibiting unique characteristics such as negative effective permittivity and permeability. Due to these distinctive characteristics, metamaterials have drawn special attention in designing novel antenna structures and improving antenna performances. The application of metamaterial in antenna technology significantly brings miniaturization to the antenna structure, enhances the impedance bandwidth, gain, and efficiency of the antenna as well as improves isolation between the MIMO antenna elements. The substrate integrated waveguide (SIW) reduces the conductor and dielectric loss, and surface wave excitations in the antennas. Although an overview of the performance enhancement of microstrip patch antennas under the influence of metamaterial has been incorporated in this article, the authors have put more effort in presenting a detailed study on working mechanism of metamaterial-based SIW antennas. Thus, a detailed review of the novel designs of metamaterial-inspired SIW cavity-backed slot antennas (CBSA), leaky-wave antennas (LWA), aperture antennas, and  $H$ -plane horn antennas has been included. The theoretical background of the metamaterials characteristics has been presented. Moreover, the working principles of metamaterial-based SIW CBSAs, SIW LWAs, SIW aperture antennas, and SIW  $H$ -plane horn antennas have been thoroughly outlined in obtaining antenna miniaturization, gain enhancement, beam steering through frequency scanning, polarization flexibility, bandwidth broadening, and isolation improvement. Besides this, a study has also been included in eliminating the limitations of SIW on-chip antennas such as narrow bandwidth, low gain, and efficiency by including metamaterial/metasurface in the antenna designs. Although the emphasis has been given to elaborating the attractive antenna performances, some design limitations have also been identified, and those need further investigation. This survey brings up not only the conceptual framework of the attractive characteristics of metamaterial, the design methodology of the non-resonant type metamaterial in the SIW environment, and the working principles of metamaterial-inspired SIW antennas but also the design limitations. Thus, consideration can be given to this article as the potential design guidelines of the metamaterial-based SIW antennas, and possible ideas can be obtained for doing further advanced research on the identified research gaps.

## 1. INTRODUCTION

The modern antenna technology for high-speed wireless communication relies on compact antenna profile. Low-profile antennas are suitable to integrate with other electronic components or microwave devices in wireless system's hardware. Low-profile antennas are also helpful in reducing the overall dimensions of mobile, airborne, and IoT devices, and it is well suited in a limited space. Typically, the microstrip patch antennas (MPA) [1–3] can be considered as an appropriate choice in using as compact and low-profile antennas. Although the MPAs are miniaturized antennas, they encounter low

---

*Received 24 May 2022, Accepted 9 August 2022, Scheduled 24 August 2022*

\* Corresponding author: Wriddhi Bhowmik (Wriddhi.bhowmikfet@kiit.ac.in).

<sup>1</sup> School of Electronics Engineering, Kalinga Institute of Industrial Technology, Bhubaneswar 751024, Odisha, India. <sup>2</sup> Department of Electronics & Communication Engineering, Jaypee Institute of Industrial Technology, Noida 201309, Uttar Pradesh, India.

gain, low bandwidth, and surface wave excitation. The surface waves propagate along the antenna's substrate, and it increases the electromagnetic coupling between the antenna elements when the elements are accommodated in close proximity. Thus, the surface wave excitation causes cross-talk and also degrades the overall performance of the antenna system. These drawbacks of MPAs can be overcome by introducing artificially engineered materials named metamaterial [4, 5] in the antenna design. The unique characteristics of the metamaterial do not rely on the dielectric but on the smart structures realized on it. The attractive features of the metamaterial include not only negative effective parameters (permittivity and permeability) but also its subwavelength size. Thus, the implementation of metamaterials in MPAs' designs brings novelty in antenna structures as well as improves antenna performances. The inclusion of metamaterials in MPAs has miniaturized antenna structure as well as enhanced the antenna gain [6–10]. Metamaterials have also been introduced between array elements to reduce the surface waves excitation in the substrate so as to minimize the coupling and provide better isolation between the array elements [11–13]. Although the integration of metamaterials into the MPAs has made the antennas' performance better, still in searching of suitable alternative to MPAs, the researchers have explored the opportunity of incorporating waveguide technology in realizing leaky wave antennas, horn antennas, and antenna arrays. The waveguide technology [14] minimizes the dielectric loss, and it also provides a guided path to electromagnetic waves. Hence, this technique is useful in reducing dielectric losses in antenna as well as mitigating the crosstalk between the array elements as it confines EM waves. The waveguide transmission line exhibits wider passband, and hence, waveguide horns and leaky wave antennas can be considered as the preferable choice of wideband and high gain antennas. The non-planar structure of waveguide makes the antenna profile bulky, the process of realization costly, and the integration to the other planar microwave devices difficult, despite numerous advantages. These drawbacks of rectangular waveguide (RW) can be eliminated by a promising alternative named substrate integrated waveguide (SIW) technology. SIW is the planar implementation of non-planar RW by upholding all the merits of RW such as high Q factor [15]. SIW is a potential candidate to be used in ultra-wideband (UWB) applications. SIW based antennas such as SIW cavity-backed slot antennas, SIW leaky-wave structures, as well as SIW horn antennas are considered as a suitable alternative to MPAs to be used in the high-speed wireless communication. The design of SIW-based antennas incorporating unique features of metamaterial brings novelty as well as flexibility in SIW antenna structures.

In this article the definition of metamaterial, categorization, principle of operation and characteristics are first described followed by a complete review on the microstrip patch antennas' performances under the influence of metamaterial. An effort has been undertaken in presenting novel designs of the metamaterial-based SIW antennas that developed over the past few years in this paper. The application of metamaterial in SIW antennas to achieve antenna miniaturization, beam steering, gain enhancement, polarization flexibility, isolation improvement, bandwidth broadening, and performance improvement of SIW on-chip antennas has been thoroughly reviewed. Mainly, emphasis has been put on the working principles of metamaterial-based SIW antennas in obtaining design flexibility. The primary aim of writing this article is to represent the influence of the unique properties of the metamaterial in obtaining the attractive outcomes of the metamaterial-inspired microstrip patch and SIW antennas to the researchers.

## 2. INTRODUCTION TO SUBSTRATE INTEGRATED WAVEGUIDE (SIW)

SIW is a dielectric filled waveguide, and the narrow walls of the waveguide can be formed by rows of metallic vias to minimize the leakage loss. These rows of metallic posts form the electrical wall in order to arrest the outflow of EM waves and also to form a guided path. The width of the SIW can be calculated by using the following equation [15]

$$w_{eff} = w - 1.08 \left( \frac{d^2}{s} \right) + 0.1 \left( \frac{d^2}{w} \right) \quad (1)$$

where  $w$  is the width of SIW,  $w_{eff}$  the width of equivalent dielectric filled rectangular waveguide,  $d$  the diameter of metallic pins, and  $s$  the centre-to-centre spacing between the metallic vias. " $w_{eff}$ " can be

calculated from the formula given below [16]

$$w_{eff} = \frac{c}{2f_c\sqrt{\epsilon_r}} \tag{2}$$

where  $c$  is the speed of light,  $f_c$  the waveguide cut-off frequency, and  $\epsilon_r$  the relative permittivity of the dielectric substrate. Typically, the value of  $w_{eff}$  lies between  $w$  and  $(w - d)$  [15]. Reliable design guidelines of the SIW suggest to maintain the ratios such as  $s/d < 2$  and  $d/w < 1/5$  to minimize the leakage loss. SIW facilitates the integration of waveguide components such as waveguide couplers, waveguide slot antennas, and leaky-wave antennas with other planar devices. SIW reduces the width of conventional rectangular waveguide by a factor of  $1/\sqrt{\epsilon_r}$ . The layout of SIW and its  $S$ -parameter and dispersion characteristics are respectively presented in Figures 1, 2, and 3.

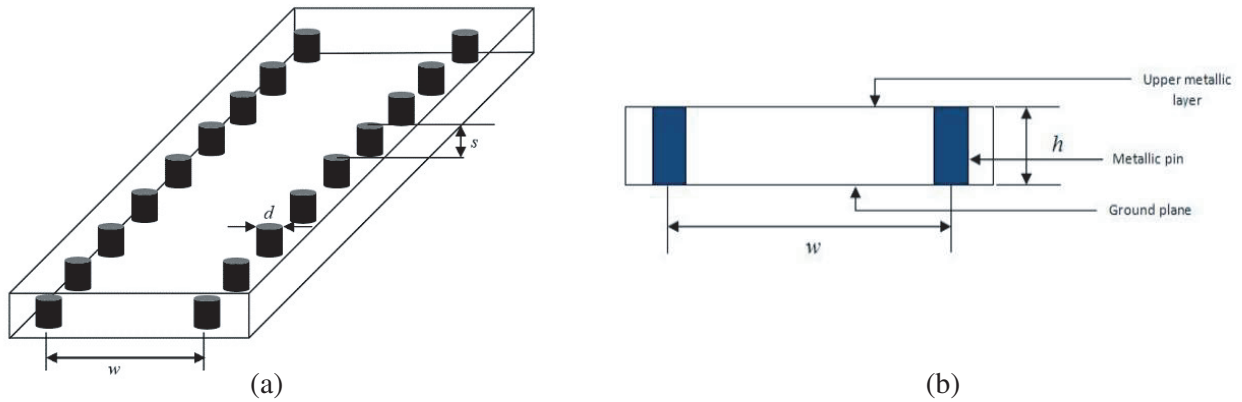


Figure 1. Layout of SIW: (a) perspective view, and (b) cross-sectional view.

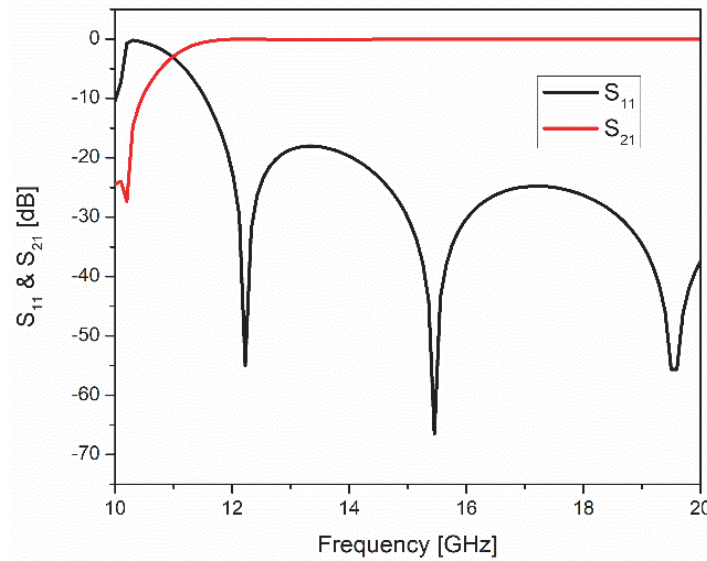
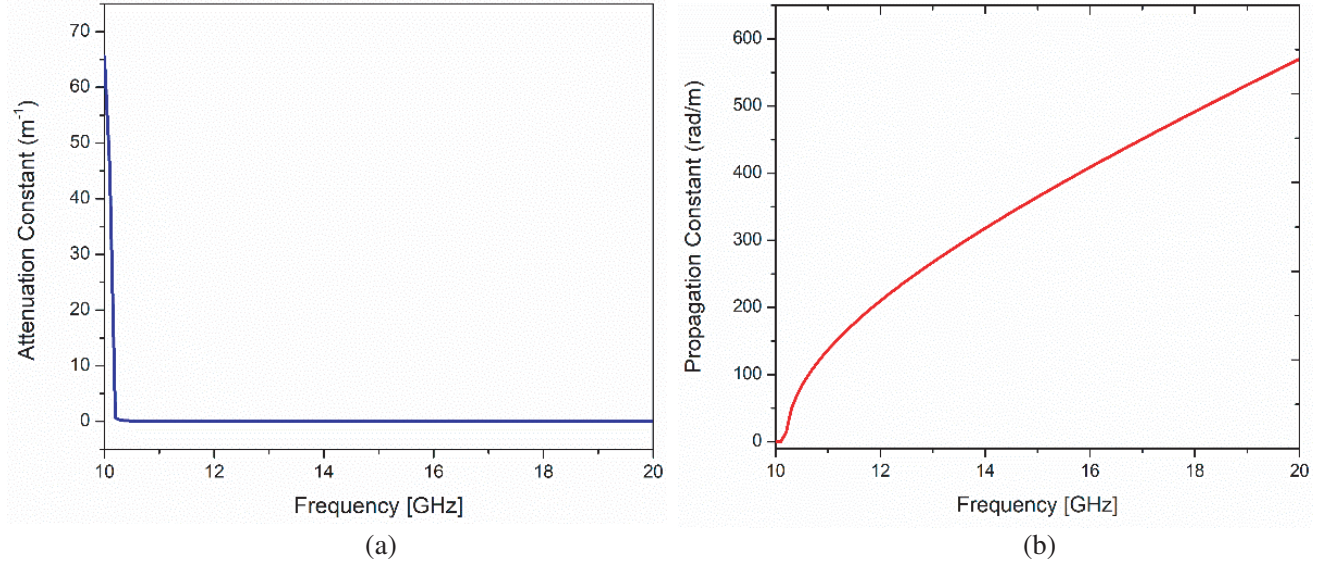


Figure 2.  $S$ -parameter characteristics of SIW.

It is evident from Figure 2 that similar to conventional rectangular waveguide, SIW also works as a high-pass filter. After the cut-off frequency (in this case it is 12 GHz), the attenuation constant decreases near zero, and the propagation constant increases with increasing frequency as observed in Figures 3(a) and 3(b), respectively. Thus, it can be stated that SIW upholds all the merits of conventional rectangular waveguide.



**Figure 3.** Dispersion characteristics of SIW: (a) attenuation constant, and (b) propagation constant.

### 3. INTRODUCTION TO METAMATERIAL

Generally, dielectric material supports forward electromagnetic (EM) wave propagation. This natural behavior of the EM wave in conventional material can be controlled by designing composite materials. Metamaterials are usually composite materials, which contain arrays of identical metallic resonators. This array repeats itself periodically. The features of metamaterial do not depend on the base material but on the resonator structures design on it. Typically, metamaterial exhibits negative permittivity ( $\epsilon < 0$ ) and permeability ( $\mu < 0$ ) [17]. Metamaterial can be categorized as Single-Negative (SNG) (either permittivity or permeability is negative), Double-Negative (DNG) (both the permittivity and permeability are negative), and Zero-Index (either permittivity or permeability is zero) materials. Presently, electromagnetic band-gap (EBG) structures and artificial magnetic conductors (AMC) are also customarily used as metamaterials [18]. Right-handed material (RHM) ( $\epsilon > 0$  and  $\mu > 0$ ) supports forward propagating wave. As per the Maxwell's equations in RHM, electric field ( $\mathbf{E}$ ), magnetic field ( $\mathbf{H}$ ), and wave vector ( $\mathbf{k}$ ) form the right-handed coordinate system. SNG materials support evanescent waves as the propagation constant is real. DNG materials are usually known as left-handed materials (LHM). In LHM, the  $\mathbf{E}$ ,  $\mathbf{H}$ , and  $\mathbf{k}$  form a left-handed coordinate system, and hence it supports the backward propagation of waves [19]. The classification of the materials has been demonstrated in  $\epsilon$ - $\mu$  diagram as observed in Figure 4. Right and Left-handed coordinate systems are presented in Figure 5. The backward propagating waves indicate that the directions of phase and group velocity are opposite to each other. In 1967, Russian scientist Veselago first theoretically demonstrated the electrodynamics of DNG/LHM and also some of its interesting properties such as negative refractive index ( $n < 0$ ), reversal of doppler effect, and left-handed propagation [20].

The realization of material with negative permittivity ( $\epsilon < 0$ ) in microwave frequency range is first presented by Sir John Pendry [21]. He showed that the periodic structure of thin metallic wires can exhibit negative permittivity below the plasma frequency. He also showed that split ring resonator (SRR) produces negative permeability ( $\mu < 0$ ) around its resonance frequency [22]. The complementary split-ring resonator (CSRR) can also take part in making metamaterial-based microwave circuitry and antennas [23]. The metallization in SRR is replaced in CSRR by air/dielectric. Hence, by Babinet's principle, it can be stated that the CSRR is dual of SRR. Thus, the resonance frequency of CSRR is identical to SRR. Unlike SRR, it possesses negative permittivity ( $\epsilon < 0$ ) [24].

Figure 6 and Figure 8 respectively represent the periodic structure of thin metallic wires and variation of effective permittivity as a function of frequency. The electric field ( $\mathbf{E}_z$ ) is applied parallel



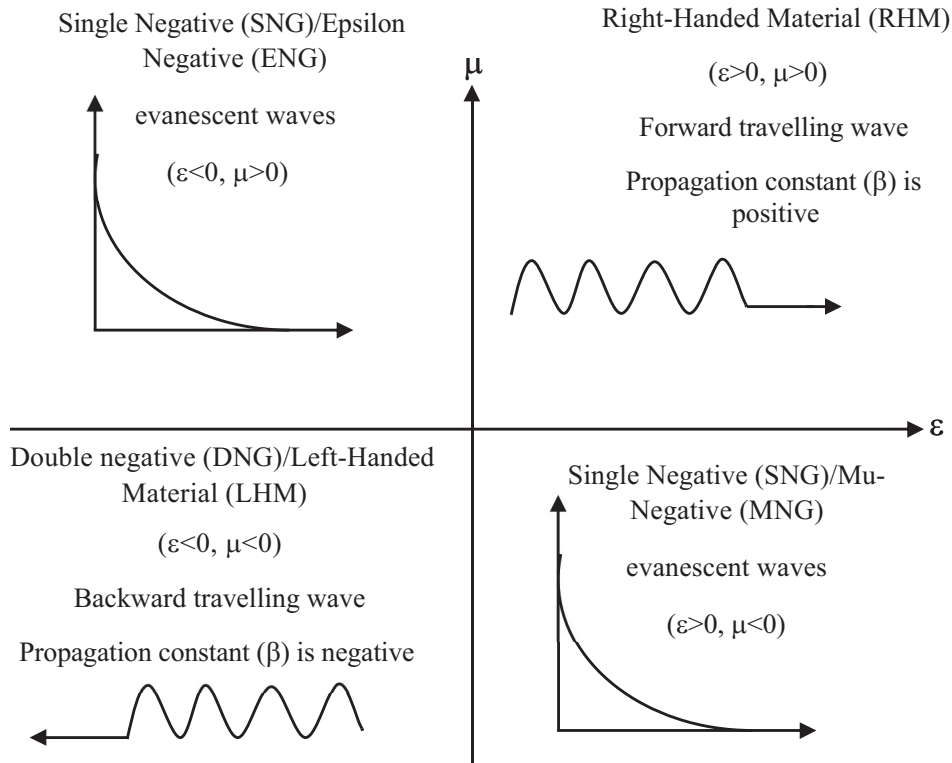


Figure 4. Permittivity-permeability ( $\epsilon$ - $\mu$ ) diagram.

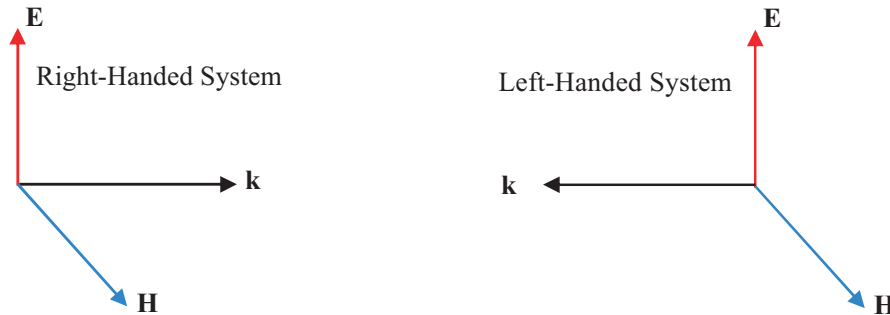
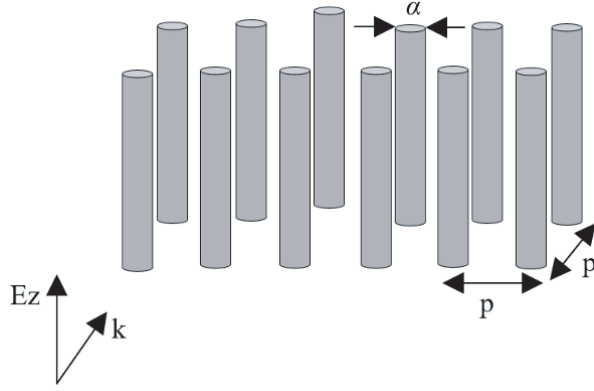
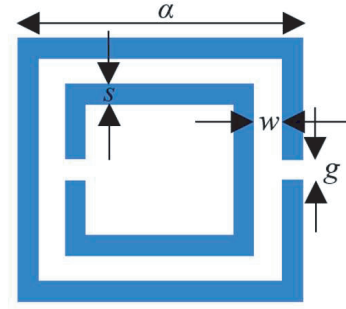


Figure 5. Right and left-handed co-ordinate system.

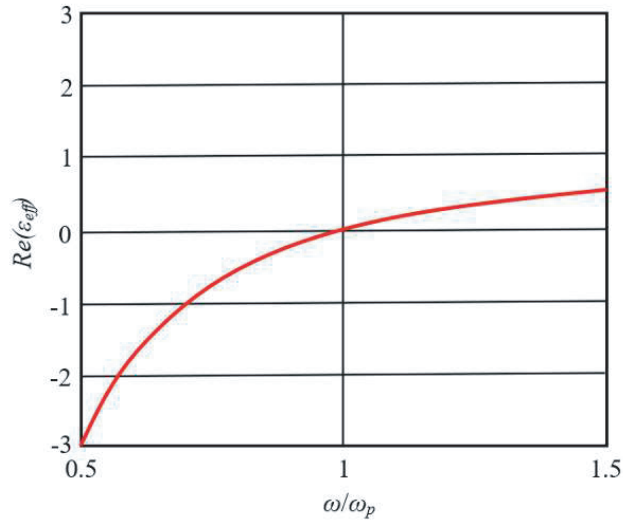
to the wires as observed in Figure 6. It is evident from Figure 6 that  $\alpha$  represents the diameter of metallic wire whereas  $p$  is the periodicity. The procedure to calculate effective permittivity as a function frequency ( $\epsilon_{eff}(\omega)$ ) has been presented in [18]. The periodic thin metallic wires have made the real part of effective permittivity negative below the plasma frequency ( $\omega_p$  is the plasma frequency), as observed in Figure 8. Figure 7 represents the unit cell of SRR, which contains two square shaped metallic rings with a spacing ( $w$ ) between them. The current is induced on the conducting rings of SRR, when an external time varying magnetic field is applied perpendicular to the SRR's surface. Due to the current flow in the metallic rings, charges are accumulated across the gaps between the rings. Thus, the SRR can be approximated by a parallel  $LC$  circuit (tank circuit), whose resonance frequency can be given as  $f_0 = 1/2\pi\sqrt{LC}$ . The inductance  $L$  and capacitance  $C$  come in the scenario respectively due to the metallic rings and gaps between them. The effective permeability ( $\mu_{eff}(\omega)$ ) of the single SRR unit has been reported in [18]. The SRR makes the real part of  $\mu_{eff}(\omega)$  negative for a narrow bandwidth around the resonance ( $\omega_m$ ) as observed in Figure 9. Negative permeability bandwidth can be enhanced



**Figure 6.** Periodic structure of thin metallic wires, possesses negative permittivity ( $\epsilon < 0$ ). Original figure is available in [18].



**Figure 7.** Split ring resonator (SRR) unit cell, possesses negative permeability ( $\mu < 0$ ). Original figure is available in [18].



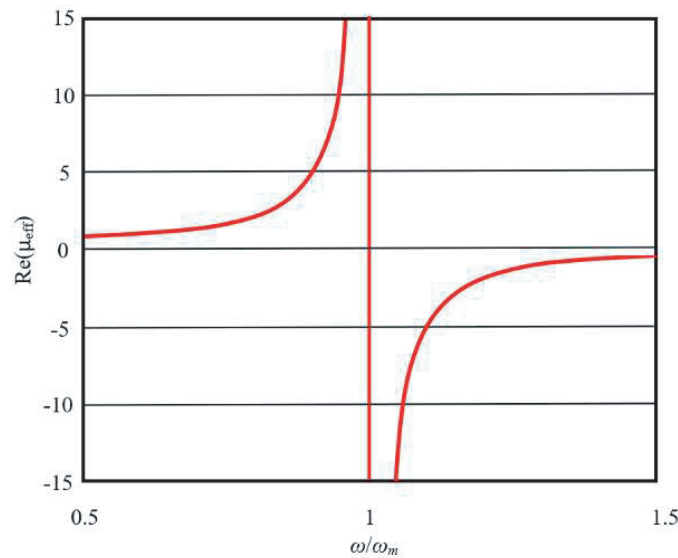
**Figure 8.** Behavior of effective permittivity of periodic thin metallic wires. Original figure is available in [18].

by repeating the single SRR unit periodically.

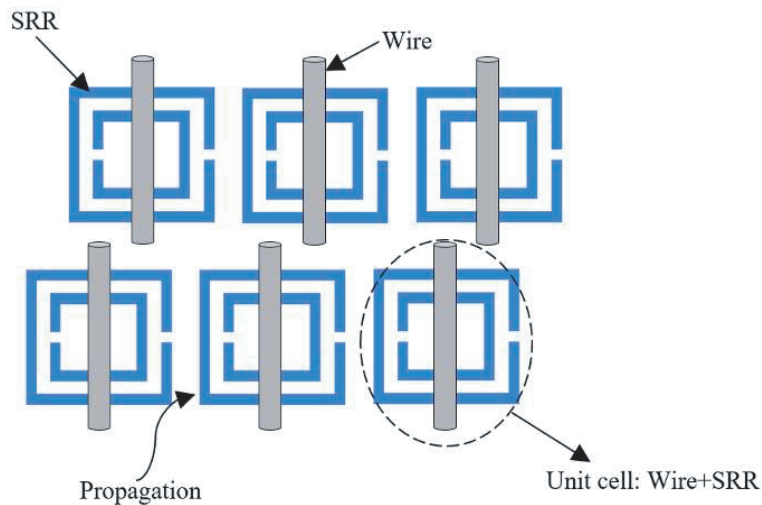
Double-negative (DNG)/left-handed materials (LHM) can be formed in the combination of epsilon-negative (ENG) and mu-negative (MNG) materials. An approach of realizing LHM has been reported in [25]. The unit cell of LHM consists of a thin metallic wire and SRR as observed in [25]. The making of unit cell has been accomplished by placing the wire in front of SRR as observed in Figure 10. It has also been observed from Figure 10 that the periodic repetition of the unit cells completes the design of LHM. The resonance frequency of SRR should be tuned lower than the plasma frequency of thin wire to obtain negative permittivity and permeability simultaneously.

### 3.1. Design Approach of Metamaterials

There are two approaches available in designing metamaterials namely resonant approach and transmission line approach. Resonant approach includes the utilization of thin metallic wires, SRRs, and CSRRs. Transmission line approach depends on the dual transmission line theory [26]. Resonant approach makes the circuits lossy and its bandwidth narrow, whereas transmission line approach is non-resonant type and eliminates the drawbacks associated with the former.



**Figure 9.** Behavior of effective permeability of single SRR unit. Original figure is available in [18].

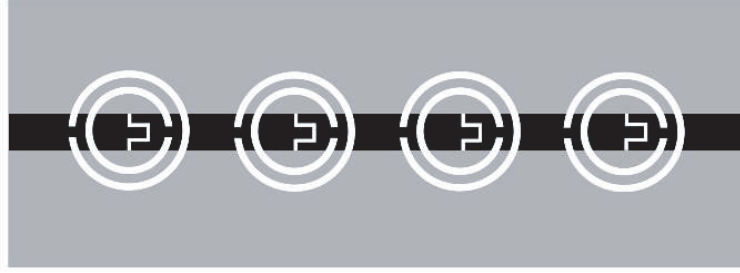


**Figure 10.** Layout of DNG/LHM. Concept is available in [25]. Original figure is available in [18].

### 3.1.1. Resonant Approach

Typically, SRRs are metallic rings and could be of any shape and incorporated near the microstrip line. Although it produces negative permeability over a narrow bandwidth, the SRR based circuits have gained lots of recognition to the researchers. Unlike SRR, CSRRs are etched in the ground plane and can be accommodated beside the microstrip line or beneath of it. Similar to SRR, CSRR can also be used to realize SNG materials. Unlike SRR, CSRR makes the permittivity negative ( $\epsilon < 0$ ). The periodic arrangement of CSRR in the ground plane (beneath the microstrip line) and the incorporated periodic gaps in the microstrip line together produce purely LH (left-handed) behavior over a narrow frequency band.

Circular ring-shaped CSRRs have been periodically etched beneath the microstrip line in the ground plane as observed in Figure 11. Some gaps have also been etched in the microstrip line (capacitive gaps). The CSRR in the ground plane and capacitive gaps in the microstrip line together produce LH response.

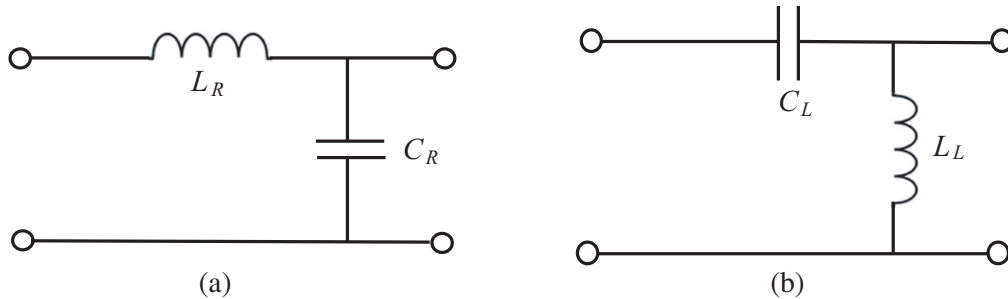


**Figure 11.** Layout of composite structure to obtain purely LH behavior. Original figure is available in [24].

### 3.1.2. Transmission Line Approach

Subwavelength size (typically  $\lambda/10$ ) of SRRs and CSRRs is responsible for the high loss and narrow band performance of microwave circuits. Non-resonant transmission line (TL) approach eliminates these drawbacks. Thus, the researchers have considered this TL approach as a suitable alternative in designing metamaterials. Typically, a lossless (dielectric and conductor loss are not considered) right-handed (RH) TL consists of a series inductor ( $L_R$ ) and shunt capacitor ( $C_R$ ). Left-handed (LH) TL is dual of RH-TL, and hence it comprises series capacitor ( $C_L$ ) and shunt inductor ( $L_L$ ).

The unit cell of typical RH and LH TLs is presented in Figures 12(a) and 12(b), respectively. It has been observed by the researchers that the existence of pure LH-TL is impractical as the presence of parasitic series inductance and shunt capacitance is unavoidable. Thus, by introducing an additional series inductance ( $L_R$ ) and shunt capacitance ( $C_R$ ) in LH-TL, a unit cell of composite right/left-handed (CRLH-TL) transmission line can be formed. The dispersion characteristics of CRLH-TL has been modified. The unit cell of CRLH-TL exhibits positive and negative phase constants for some frequency bands along with a stopband.

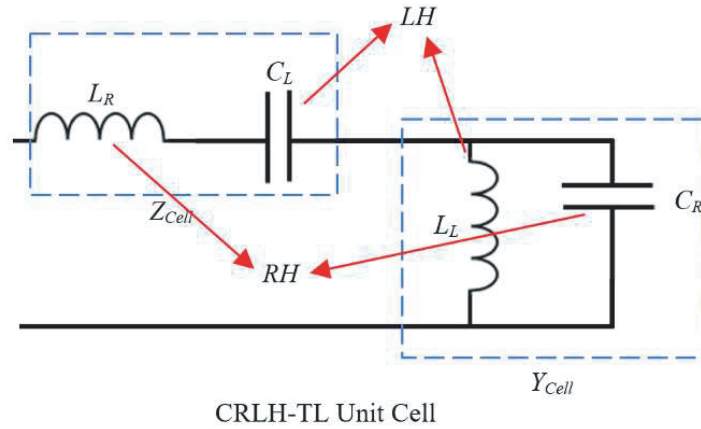


**Figure 12.** (a) Unit cell of RH-TL and (b) unit cell of LH-TL.

The unit cell of CRLH-TL is presented in Figure 13. The propagation constant of CRLH-TL unit cell is given as  $\gamma = \alpha + j\beta = \sqrt{Z_{Cell}Y_{Cell}}$  [18], where  $\alpha$  is the attenuation, and  $\beta$  is the phase constant. The impedance ( $Z_{Cell}$ ) due to the series combination of inductance ( $L_R$ ) and capacitance ( $C_L$ ) in the unit cell of CRLH-TL as well as admittance ( $Y_{Cell}$ ) for the parallel combination of inductance ( $L_L$ ) and capacitance ( $C_R$ ) have been formulated in [18], and it can be given as follows

$$Z_{Cell}(\omega) = j \left( \omega L_R - \frac{1}{\omega C_L} \right) \quad (3)$$

$$Y_{Cell}(\omega) = j \left( \omega C_R - \frac{1}{\omega L_L} \right) \quad (4)$$



**Figure 13.** Unit cell of composite right/left-handed transmission line (CRLH-TL). Original figure is available in [18].

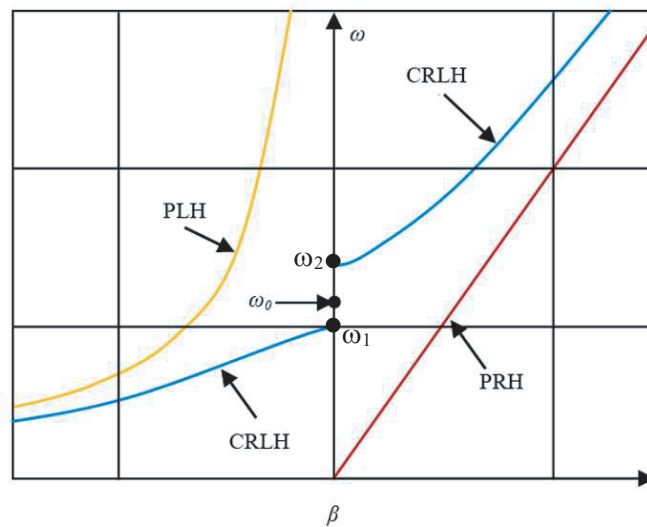
The phase constant  $\beta(\omega)$  can be calculated as follows [18]

$$\beta(\omega) = s(\omega) \sqrt{\omega^2 L_R C_R + \frac{1}{\omega^2 L_L C_L} - \left( \frac{L_R}{L_L} + \frac{C_R}{C_L} \right)} \quad (5)$$

where,  $s(\omega) = -1$ , if  $\omega < \omega_1 = \min \left( \frac{1}{\sqrt{L_R C_L}}, \frac{1}{\sqrt{L_L C_R}} \right)$  (6)

and  $s(\omega) = +1$ , if  $\omega > \omega_2 = \max \left( \frac{1}{\sqrt{L_R C_L}}, \frac{1}{\sqrt{L_L C_R}} \right)$  (7)

It is observed from Figure 14 that the phase constant is negative for  $\omega < \omega_1$ , and it is positive for  $\omega > \omega_2$ . Thus, it can be stated that the CRLH-TL exhibits LH-TL behavior below the frequency  $\omega_1$  and RH-TL behavior above the frequency  $\omega_2$ . Careful observation on the dispersion characteristics of CRLH-TL (Figure 14) notifies that it does not produce pure LH and RH behaviors in LH and RH



**Figure 14.** Comparison of dispersion characteristics of purely right-handed transmission line (PRH-TL), purely left-handed transmission line (PLH-TL), and composite right/left-handed transmission line (CRLH-TL). Original figure is available in [18].

regimes, respectively. The presence of parasitic RH series inductance ( $L_R$ ) and shunt capacitance ( $C_R$ ) (Figure 13) causes this discrepancy in the LH behavior in comparison to the pure LH propagation characteristics. Hence, proper justification to this type of LH behavior (highlighted in blue color in Figure 14) can be done by introducing CRLH-TL. A clear bandgap of  $\omega_2-\omega_1$  has been observed in the dispersion properties of CRLH-TL, which can be minimized by proper selection of series and shunt capacitances and inductances values of the unit cell. The transition from LH to RH domain occurs at the frequency  $\omega_0$ , and it is given by [18]

$$\omega_0 = \sqrt[4]{\frac{1}{C_R L_R C_L L_L}} \quad (8)$$

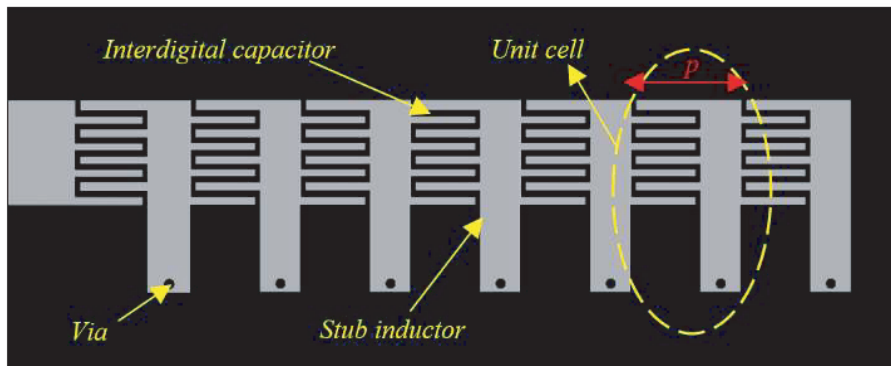
At  $\omega_0$  frequency, the propagation constant is zero as observed in Figure 14. The effective permittivity and permeability of CRLH-TL are given as follows [18]

$$\varepsilon_{eff}(\omega) = L_R - \frac{1}{\omega^2 C_L} \quad (9)$$

$$\mu_{eff}(\omega) = C_R - \frac{1}{\omega^2 L_L} \quad (10)$$

These effective parameters (Eq. (9) and Eq. (10)) of CRLH-TL are both negative in the LH frequency region, and it acts as a DNG material (metamaterial). One of these parameters is negative in the bandgap, and both are positive in the RH frequency region. Hence, the CRLH-TL acts as an SNG material in the bandgap and as a right-handed material (RHM) in RH frequency regime. The realization of CRLH-TL can be obtained by periodical incorporation of interdigital capacitor in series as series capacitance ( $C_L$ ), and grounded stubs as shunt inductance ( $L_L$ ), to the RH-TL.

The practical implementation of composite right/left-handed transmission line (CRLH-TL) metamaterial using distributed element is presented in Figure 15. The unit cell of CRLH-TL metamaterial consists of an interdigital capacitor and a stub inductor, which are integrated to an RH-TL. The periodical repetition ( $p$ ) of the unit cells completes the whole structure of CRLH-TL metamaterial, as depicted in Figure 15. The metallization of CRLH-TL metamaterial is indicated by the grey shade in Figure 15. This design of CRLH-TL metamaterial constitutes wide band and low loss double negative/left-handed (DNG/LH) metamaterials, as compared to the periodic arrangement of combined SRRs and thin wires. Also, it is suitable to integrate with other microwave components.



**Figure 15.** Realization of CRLH-TL metamaterial using distributed element. Original figure is available in [18].

### 3.2. Application of Metamaterial in Designing of Microstrip Patch Antennas

A rigorous study of metamaterial application in microstrip patch antenna designing has been reported in [27]. It has been observed that the metamaterial is quite often used in antenna miniaturization [28–46], performance improvement of on-chip antennas in THz frequency band [47, 48], designing of impedance



matching network [49, 50], microwave imaging [51], and mutual coupling reduction in MIMO and SAR antennas [52–62]. Some of the examples of antenna performances under the influence of metamaterial have been listed in the table below (Table 1).

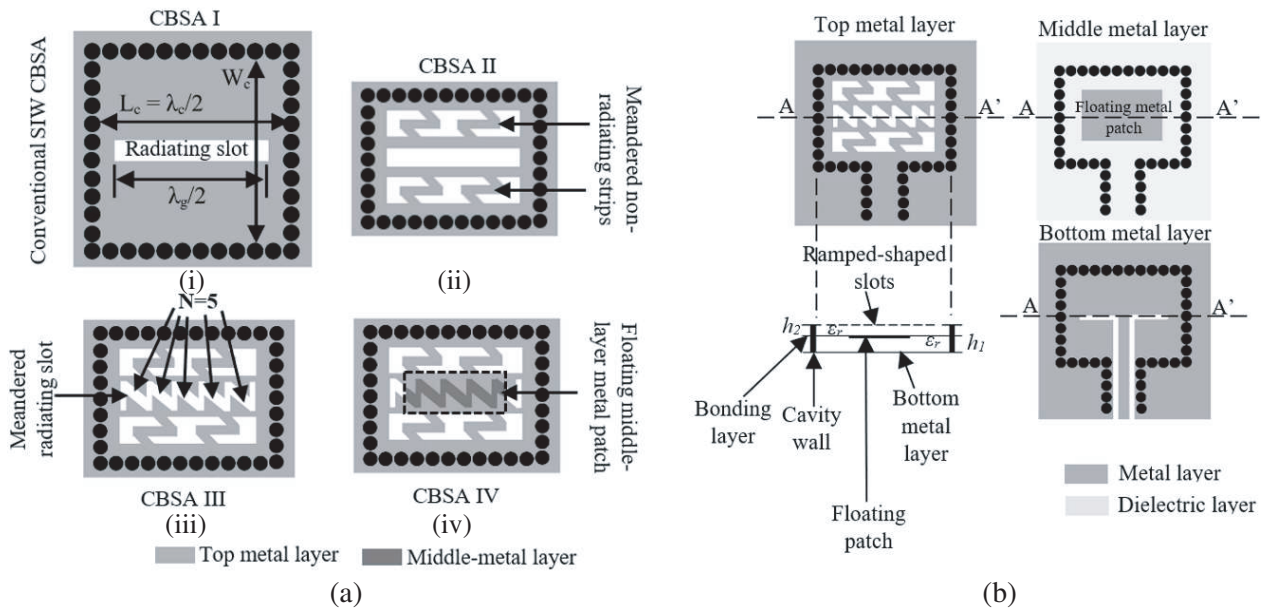
It is observed from Table 1 that the metamaterial has significant contribution in designing wideband miniaturized antennas as well as in enhancing isolation between the array elements in MIMO antennas. Quite interesting characteristics of metamaterial-inspired microstrip antennas have influenced the researchers in continuing research to obtain similar attractive features by designing metamaterial-based SIW antennas. The next section of this article includes a thorough survey on metamaterial-based SIW antennas. Specifically, the following discussion includes the working principle of metamaterial-inspired SIW antennas in obtaining attractive antenna behavior.

#### 4. APPLICATION OF METAMATERIALS IN SUBSTRATE INTEGRATED WAVEGUIDE (SIW) ANTENNAS

This section presents a review of several kinds of research which have already been carried out on metamaterial-based SIW cavity backed slot antennas,  $H$ -plane horn antennas, aperture antennas, and leaky-wave antennas.

##### 4.1. Antenna Miniaturization

An ultra-miniaturized SIW cavity backed slot antenna has been reported in [63]. The width of the SIW cavity has been reduced by incorporating non-radiative meandered strip line around a rectangular radiating slot. The metallic plane around the radiating slot can be replaced by a meandered strip line of similar effective length. The replacement of uniform metallic plane has been done in such a way that the required surface current could be maintained on the metallic plane. The reference SIW CBSA is presented in Figures 16(a)-(i). In [63], two ramp-shaped meandered strip lines have been



**Figure 16.** (a)-(i) Conventional SIW cavity backed slot antenna, (a)-(ii) size reduction (especially the width of the cavity) using non-radiating meandered strip line, (a)-(iii) size reduction (especially the length of the radiating slot and cavity) by replacing conventional radiating rectangular slot with a radiating interdigital slot, (a)-(iv) incorporation of floating metallic patch beneath the radiating ramp-shaped slots for maximum miniaturization (miniaturization in the length of the radiating slot and cavity), and (b) layout of the optimal design. Original figures are available in [63].

**Table 1.** Performance analysis of the metamaterial-inspired microstrip antennas.

Application of Metamaterial in Miniaturization & Wide-band performance of the Antenna					
Reference	Design Technique & Process	Operating Frequency Band (GHz)	Antenna Dimensions	Antenna Fractional Bandwidth (FBW)	Antenna Gain (dBi)
[28]	CRLH-TL metamaterial & Microstrip	1–3.2	$0.047\lambda_0 \times 0.021\lambda_0 \times 0.002\lambda_0$ at 1 GHz.	104.76	2.3 dBi at 2.1 GHz.
[29]	Simplified CLRH-TL Metamaterial & Microstrip	0.65–9.2	$0.054\lambda_0 \times 0.032\lambda_0 \times 0.003\lambda_0$ at 0.65 GHz	173.6%	3.5
[30]	CRLH-TL metamaterial & Microstrip	0.93–3.65	$0.059\lambda_0 \times 0.047\lambda_0 \times 0.004\lambda_0$ at 0.93 GHz.	118.7%	8
[31]	CRLH-TL metamaterial & Microstrip	H-shaped slits: 1.2–6.7 T-shaped slits: 1.1–6.85	H-shaped slits: $0.06\lambda_0 \times 0.02\lambda_0 \times 0.003\lambda_0$ at 1.2 GHz. T-shaped slits: $0.05\lambda_0 \times 0.02\lambda_0 \times 0.002\lambda_0$ at 1.1 GHz.	H-shaped slits: 139% T-shaped slits: 144%	H-shaped slits: 2–6.8 (over entire operating BW). T-shaped slits: 2–7.1 (over entire operating BW)
[32]	Simplified CLRH-TL Metamaterial & Microstrip	0.7–8	$0.0504\lambda_0 \times 0.0462\lambda_0 \times 0.0018\lambda_0$ at 0.7 GHz.	167.81%	4 dBi at 4.75 GHz, and 3.6 dBi at 7 GHz.
[33]	CRLH-TL metamaterial & Microstrip	5.8–7.3	$0.39\lambda_0 \times 0.13\lambda_0 \times 0.015\lambda_0$ at 5.8 GHz.	23%	4.8 dBi at 6.6 GHz.
[34]	CRLH-TL metamaterial & Microstrip	Antenna with 2-unit cells: 500 MHz–1.35 GHz. Antenna with 3-unit cells: 650 MHz–1.85 GHz.	Antenna with 2-unit cells: $0.017\lambda_0 \times 0.006\lambda_0 \times 0.001\lambda_0$ at 500 MHz. Antenna with 3-unit cells: $0.028\lambda_0 \times 0.008\lambda_0 \times 0.001\lambda_0$ at 650 MHz.	Antenna with 2-unit cells: 91.9%. Antenna with 3-unit cells: 96%.	Antenna with 2-unit cells: 5.3 dBi. Antenna with 3-unit cells: 5.7 dBi.
[35]	CRLH-TL metamaterial & Microstrip	165 MHz–875 MHz	$0.0302\lambda_0 \times 0.0357\lambda_0 \times 0.0008\lambda_0$ at 165 MHz.	136.5%	1.2 dBi at 400 MHz.
[36]	CRLH-TL metamaterial & Microstrip	0.5–11.3	$0.037\lambda_0 \times 0.009\lambda_0 \times 0.0001\lambda_0$ at 0.5 GHz.	183%	6.5 dBi at 8 GHz.
[37]	CRLH-TL metamaterial & Microstrip	0.8–6.05	$0.056\lambda_0 \times 0.04\lambda_0 \times 0.002\lambda_0$ at 0.8 GHz.	153.28%	5.35 dBi at 4.45 GHz.
[38]	CRLH-TL metamaterial & Microstrip	0.4–4.7	$0.017\lambda_0 \times 0.006\lambda_0 \times 0.002\lambda_0$ at 0.4 GHz.	170%	2 dBi at 2.5 GHz.
[39]	Simplified CLRH-TL Metamaterial & Microstrip	0.3–4.15	Not available	173%	4.8 dBi at 2.4 GHz
[40]	Resonant type, Split ring resonator (SRR), & Microstrip	F-shaped monopole with SRR: 2.9–6.41. T-shaped monopole with SRR: 2.6–6.6.	F-shaped and T-shaped monopole antennas loaded with SRR: $0.29\lambda_0 \times 0.21\lambda_0 \times 0.01\lambda_0$ at 2.9 GHz.	F-shaped monopole with SRR: 75.4%. T-shaped monopole with SRR: 87%	F-shaped monopole with SRR: 4 dBi at 6 GHz. T-shaped monopole with SRR: 4.4 dBi at 6 GHz.
[41]	CRLH-TL metamaterial & Microstrip	L-shaped metamaterial antenna: 0.2–1.8. F-shaped metamaterial antenna: 0.11–2.1.	L-shaped metamaterial antenna: $0.0089\lambda_0 \times 0.0032\lambda_0 \times 0.00053\lambda_0$ at 0.2 GHz. F-shaped metamaterial antenna: $0.0053\lambda_0 \times 0.0016\lambda_0 \times 0.00058\lambda_0$ at 0.11 GHz.	L-shaped metamaterial antenna: 160%. F-shaped metamaterial antenna: 180.1%.	L-shaped metamaterial antenna: 3.4 dBi at 1.55 GHz. F-shaped metamaterial antenna: 4.5 dBi at 1.9 GHz.
[42]	Complementary artificial magnetic conductor (CAMC), & Microstrip	0.41–4.1	$0.054\lambda_0 \times 0.047\lambda_0 \times 0.0021\lambda_0$ at 0.41 GHz.	165.84%	4.45 dBi at 2.76 GHz.
[43]	CRLH-TL metamaterial & Microstrip	0.48–6.5	$0.037\lambda_0 \times 0.027\lambda_0 \times 0.002\lambda_0$ at 0.48 GHz.	172.49%	3.7 dBi at 3.25 GHz.
[44]	Resonant type, Split ring resonator (SRR), & Microstrip	0.115–2.9	$0.235\lambda_0 \times 0.211\lambda_0 \times 0.003\lambda_0$ at 1.45 GHz.	185%	2.35 dBi at 1.45 GHz.
[45]	CRLH-TL metamaterial & Microstrip	55–65	$3.43\lambda_0 \times 1.1\lambda_0 \times 0.29\lambda_0$ at 55 GHz.	16.7%	7.8 dBi at 62 GHz.
[46]	Simplified CRLH-TL Metamaterial & Microstrip	0.5–6.4	$0.0452\lambda_0 \times 0.0627\lambda_0 \times 0.0026\lambda_0$ at 0.5 GHz.	171%	5.3 dBi at 4.4 GHz.

Application of Metamaterial/Metasurface in On-chip Antenna Design in THz Frequency Band					
Reference	Design Technique & Process	Operating Frequency Band (THz)	Antenna Dimensions	Antenna Fractional Bandwidth (FBW)	Antenna Gain (dBi)
[47]	Metasurface & Microstrip; Standard CMOS-Silicon Technology	0.5–0.56 (60 GHz)	$200 \times 200 \times 45 \mu\text{m}^3$	11.3%	5.3 dBi at 540 GHz.
[48]	Microstrip, Standard 120- $\mu\text{m}$ Silicon Technology	0.29–0.316 (26 GHz)	$20 \times 3.5 \times 0.126 \text{mm}^3$	Not available	11.71 dBi at 0.3 THz.

Application of Metamaterial/Metasurface in Designing Antenna's Impedance Matching Network for RF Front-End-Circuits								
Reference	Design Technique & Process	Reference Antenna Bandwidth (GHz)	Impedance Bandwidth of the Network/ Antenna with Matching Network	Bandwidth Improvement	Antenna Fractional Bandwidth (FBW)	Loss Induced by the Matching Network	Antenna Gain without Matching Network (dBi)	Antenna Gain with Matching Network (dBi)
[49]	Metasurface & Microstrip	Not available	BW of matching network: 1–2 (1 GHz)	Not available	Not available	0.2 dB, 5% loss in incident power.	Not available.	Not available.
[50]	CRLH-TL Metamaterial & Microstrip	0.1	BW of antenna with matching network: 3.15–5.25 (2.1 GHz).	2 GHz	52.5	Not available	5.5 dBi at 4 GHz.	8.2 dBi at 4 GHz. Improvement of 2.7 dBi.

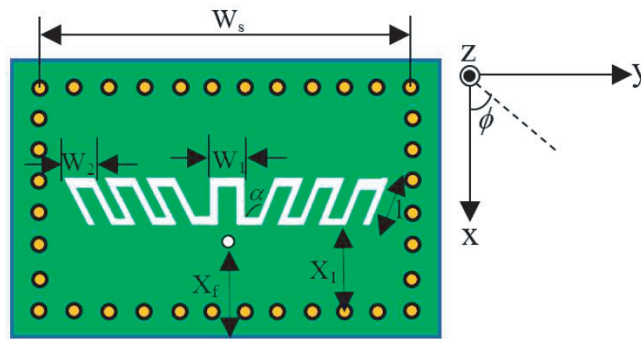
Application of Metamaterial in Antenna Design for Microwave Imaging System of Tumor Detection							
Reference	Design Technique & Process	Antenna Array Bandwidth (GHz)	Isolation between the Array Elements	Reference Antenna Gain (dBi)	Proposed Antenna Array Gain (dBi)	Radiation Efficiency of Reference Antenna	Radiation Efficiency of the Proposed Antenna Array
[51]	Metamaterial & Microstrip	2–12 (10 GHz)	Average isolation: –26 dB over the band 2 GHz–12 GHz. Maximum isolation: –43 dB at 5.5 GHz.	Standard square patch: 9.1 dBi at 12 GHz.	12 dBi at 9 GHz.	64% at 12 GHz.	81% at 9 GHz.

Application of Metamaterial/Metasurface in Minimizing Mutual Coupling in MIMO and SAR Antennas						
Reference	Design Technique & Process	Operating Frequency Band (GHz)	Maximum Isolation without Metamaterial /Metasurface	Maximum Isolation with Metamaterial /Metasurface	Isolation improvement	Antenna Gain (dBi)
[53]	Metasurface & Microstrip	139–141 (2 GHz)	$S_{12} = -50$ dB at 139 GHz	$S_{12} = -63.5$ dB at 139 GHz	13.5 dB	8.93 dBi at 141 GHz.
[54]	Microstrip	X-Band: 11.3–11.58. 1 <sup>st</sup> Ku-Band: 13.1–14.28. 2 <sup>nd</sup> Ku-Band: 15.48–17.1. 3 <sup>rd</sup> Ku-Band and K-Band: 17.8–22.5.	X-Band: $-24$ dB at 11.36 GHz. 1 <sup>st</sup> Ku-Band: $-20$ dB at 14.28 GHz. 2 <sup>nd</sup> Ku-Band: $-34.4$ dB at 15 GHz. 3 <sup>rd</sup> Ku-Band and K-Band: $-31.6$ dB at 17.9 GHz.	X-Band: $-45.7$ dB at 11.36 GHz. 1 <sup>st</sup> Ku-Band: $-32.63$ dB at 14.28 GHz. 2 <sup>nd</sup> Ku-Band: $-45.6$ dB at 15 GHz. 3 <sup>rd</sup> Ku-Band and K-Band: $-46.4$ dB at 17.9 GHz.	X-Band: 21.7 dB. 1 <sup>st</sup> Ku-Band: 12.6 dB. 2 <sup>nd</sup> Ku-Band: 11.2 dB. 3 <sup>rd</sup> Ku-Band and K-Band: 14.8 dB.	8.2 dBi at 11.3 GHz.
[55]	Metamaterial based on Electromagnetic Bandgap (EBG) structure & Microstrip	8–9.25 (1.25 GHz)	$S_{12} = -21$ dB at 8 GHz. $S_{13} = -20$ dB at 9.25 GHz. $S_{14} = -20$ dB at 8.3 GHz.	$S_{12} = -38$ dB at 9.25 GHz. $S_{13} = -57$ dB at 8.27 GHz. $S_{14} = -37$ dB at 8.85 GHz.	$S_{12} = 17$ dB $S_{13} = 37$ dB $S_{14} = 17$ dB	4 dBi–7 dBi over the band of 8 GHz–9.25 GHz.
[56]	Metamaterial -Photonic Bandgap Structure (PBG) & Microstrip	9.25–11 (1.75 GHz)	$S_{12} = -12$ dB $S_{13} = -12$ dB $S_{14} = -13$ dB $S_{34} = -10$ dB $S_{35} = -22$ dB $S_{36} = -23$ dB	$S_{12} = -17$ dB $S_{13} = -18$ dB $S_{14} = -27$ dB $S_{34} = -20$ dB $S_{35} = -32$ dB $S_{36} = -42$ dB	$S_{12} = 5$ dB $S_{13} = 6$ dB $S_{14} = 14$ dB $S_{34} = 10$ dB $S_{35} = 10$ dB $S_{36} = 19$ dB	7.85 dBi at 10.6 GHz.
[57]	Metamaterial based on Electromagnetic Bandgap (EBG) structure & Microstrip	X Band: 8.7–11.7 1st Ku Band: 11.9–14.6 2nd Ku Band: 15.6–17.1 K Band: 22–26 Ka Band: 29–34.2	Not available	Not available	X Band: 37 dB 1st Ku Band: 21 dB 2nd Ku Band: 12 dB K Band: 20 dB Ka Band: 31 dB	9.15
[58]	Metamaterial based on Electromagnetic Bandgap (EBG) structure & Microstrip	9.12–9.96 (880 MHz)	$S_{12}$ & $S_{34} = -21.85$ dB at 9.96 GHz. $S_{13}$ & $S_{24} = -37.5$ dB at 9.96 GHz. $S_{14}$ & $S_{23} = -22$ dB at 9.96 GHz.	$S_{12}$ & $S_{34} = -60$ dB at 9.18 GHz. $S_{13}$ & $S_{24} = -44.3$ dB at 9.72 GHz. $S_{14}$ & $S_{23} = -33$ dB at 9.12 GHz.	$S_{12} = 38.15$ dB $S_{13} = 7$ dB $S_{14} = 11$ dB	5.4
[59]	Metamaterial Electromagnetic Bandgap (EBG) structure & Microstrip	9.7–12.3 (2.6 GHz)	$S_{12}$ & $S_{13} = -17$ dB	$S_{12}$ & $S_{13} = -45$ dB	28 dB	6.5
[60]	Metasurface & waveguide	1.7–3.85 (2.15 GHz)	$S_{12} = -27$ dB	$S_{12} = -37$ dB	10 dB	5.75–8.6 over the band 1.7 GHz–3.85 GHz.
[61]	Metamaterial & Microstrip	9.6–10.6 (0.1 GHz)	$S_{12}$ varies between $-17$ dB to $-19$ dB over the band 9.55 GHz–10 GHz.	$S_{12}$ varies between $-23$ dB to $-30$ dB over the band 9.6 GHz–10.6 GHz.	Minimum = 6 dB Maximum = 11 dB	8.87 dBi at 10.16 GHz.
[62]	Metasurface & Microstrip	X Band: 8.41–8.7 1 <sup>st</sup> Ku Band: 13.8–14.6 2 <sup>nd</sup> Ku Band: 15.6–17.05 3 <sup>rd</sup> Ku Band, K Band, & Ka Band: 17.5–30	X Band: $-26$ dB 1 <sup>st</sup> Ku Band: $-27.13$ dB 2 <sup>nd</sup> Ku Band: $-25$ dB 3 <sup>rd</sup> Ku Band, K Band, & Ka Band: $-46.5$ dB	X Band: $-33.6$ dB 1 <sup>st</sup> Ku Band: $-36.45$ dB 2 <sup>nd</sup> Ku Band: $-30$ dB 3 <sup>rd</sup> Ku Band, K Band, & Ka Band: $-55.3$ dB	X Band: 7.6 dB 1 <sup>st</sup> Ku Band: 9.32 dB 2 <sup>nd</sup> Ku Band: 5 dB 3 <sup>rd</sup> Ku Band, K Band, & Ka Band: 8.8 dB	7.9

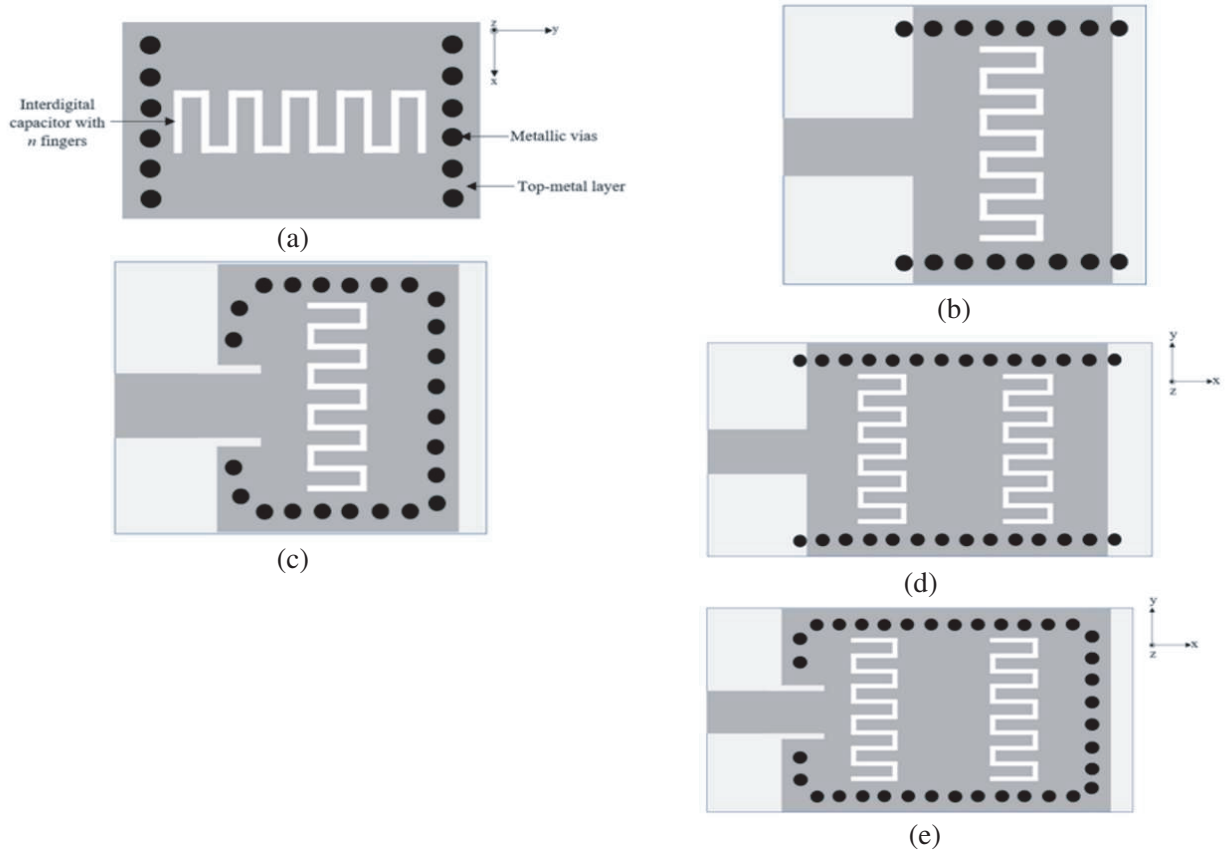
accommodated around the radiating slot to maintain the same electrical length as well as required surface current as observed in Figures 16(a)-(ii). The width of SIW cavity has been reduced, yet no change is observed in cavity length. Further miniaturization has been achieved by replacing the conventional radiating rectangular slot with ramp-shaped interdigital slots, and the design is presented in Figures 16(a)-(iii). The meandered radiating slots act as series capacitance ( $C_L$ ) and make the effective permeability negative whereas the metallic posts of SIW cavity act as shunt inductance ( $L_L$ ) and make the effective permittivity negative. Hence, the formation of CRLH-TL metamaterial has been confirmed. This technique has not further reduced the physical size of the SIW cavity backed antenna, but the resonant frequency has been lowered. The antenna has operated at  $-1^{st}$  order resonance, below the waveguide cut-off frequency. Thus, the length of the radiating slot as well as cavity has been reduced. Although adequate compactness has been obtained in antenna design, there is still a window for attaining maximum miniaturization in the design by increasing the series capacitance of the resonator circuit. The series capacitance can be increased by increasing the number of fingers ( $N$ ) in the radiating meandered slot. But the space limitation on the top metallic layer of SIW cavity has not permitted enlarging the size of ramp-shaped slots. Hence, to increase the capacitance of the resonator circuit, an additional dielectric layer (middle layer) along with a floating metallic patch has been incorporated in the SIW cavity as observed in Figures 16(a)-(iv). The floating metallic patch has been placed beneath the ramp-shaped slots. The cross-sectional view of the proposed antenna is reported in Figure 16(b), and it gives a clear idea regarding the placement of the floating patch in SIW CBSA. The inclusion of a floating metallic patch in the proposed SIW CBSA has further lowered the  $-1^{st}$  order resonance. Hence, maximum miniaturization in the length of radiating slot and cavity has been achieved. The optimal design of the antenna has been presented in Figure 16(b), and it is observed that the conductor-backed coplanar waveguide (CB-CPW) to SIW cavity transition is employed on the bottom layer of SIW cavity to excite the antenna. Finally, the miniaturization about 87% has been achieved by the proposed design as compared to the other SIW cavity-backed slot antennas available in the literature. The radiation efficiency of about 80% has also been achieved by the proposed antenna.

Unlike [63], the miniaturization of a SIW cavity backed slot antenna (CBSA) has been obtained in [64], by lowering the resonance frequency instead of reducing the width of SIW cavity. A metamaterial inspired slot has been etched on the top layer of SIW cavity. Typically, a ramp-shaped interdigital slot has been incorporated. The combination of a SIW cavity resonator and an interdigital ramp-shaped slot confirms the design of CRLH-TL metamaterial. Thus, the antenna has operated at  $-1^{st}$  order resonance, and it is below the waveguide cut-off frequency. The optimum result has been obtained by including  $N = 13$  fingers in the interdigital slot and maintaining  $\alpha = 110^\circ$ . The miniaturization of 79.74% has been obtained by the proposed design as compared to the other SIW CBSAs available in the literature. The total efficiency of 74.3% has been achieved by the proposed antenna. The layout of the antenna is presented in Figure 17.

In another approach, a CRLH SIW resonator has been formed by etching an interdigital slot on the top of a SIW metallic layer. Thus, the unit cell of CRLH-TL has included a SIW transmission line along with a transverse interdigital slot as observed in Figure 18(a). Two open ended and two short ended



**Figure 17.** Layout of CRLH-TL metamaterial based SIW CBSA. Original figure is available in [64].



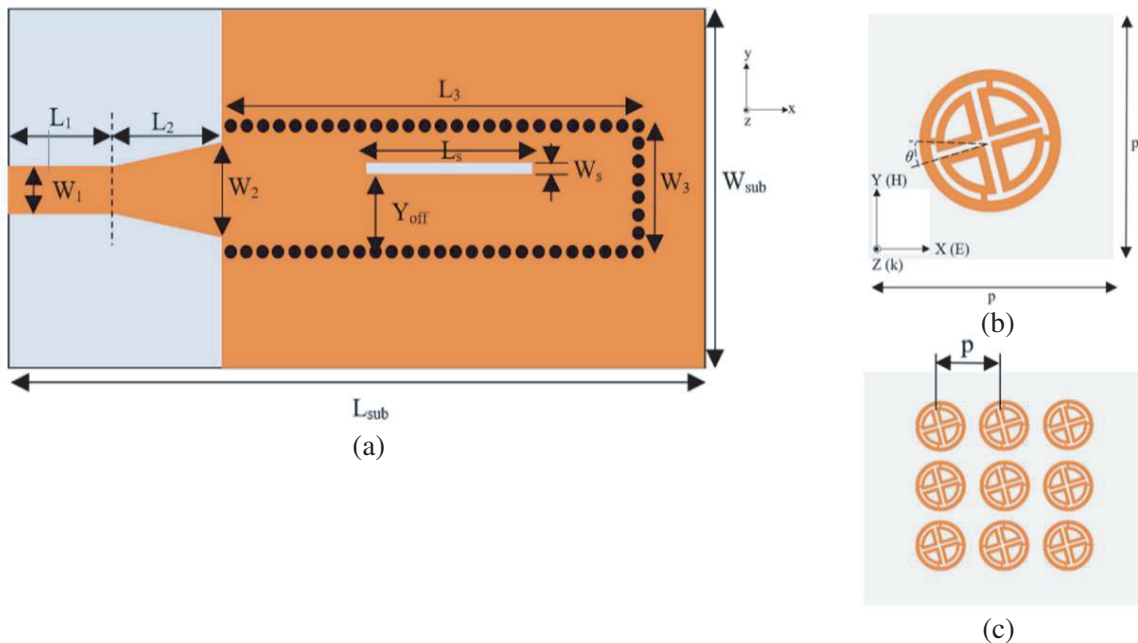
**Figure 18.** (a) CRLH-TL unit cell, (b) one-stage CRLH SIW leaky-wave antenna, (c) one-stage CRLH-TL based SIW CBSA, (d) two-stage CRLH SIW leaky-wave antenna, and (e) two-stage CRLH-TL based SIW CBSA. Original figures are available in [65].

antennas with one stage and two stage CRLH-TL unit cells have been proposed in [65]. It has been observed that the interdigital slots have worked not only as series capacitance but also as radiator, and hence, the formation of CRLH radiator is possible. The open-ended antenna with a unit [Figure 18(b)] cell has operated at  $-1^{\text{st}}$  order resonance, that is at 7.26 GHz. The cut-off frequency of SIW TL is 11.3 GHz. Thus, the miniaturization has been achieved by operating the antenna far below the cut-off frequency especially in the LH region. Similarly, the short-ended antenna [Figure 18(c)] with a unit cell, which has acted as a CRLH-TL metamaterial-based SIW CBSA, has resonated at 7.75 GHz ( $-1^{\text{st}}$  order resonance), and hence the antenna is miniaturized. The electric field's magnitude variation of the  $-1^{\text{st}}$  order resonance along the  $x$ -axis of the CRLH SIW leaky-wave antenna (Figure 8(a) in [65]) and CRLH-TL metamaterial-based SIW CBSA (Figure 10(a) in [65]) has shown that the antennas have respectively functioned as the half-wavelength and quarter-wavelength resonators. Thus, the short-ended antenna is larger in size in terms of wavelength than the open-ended antenna. The open-ended CRLH antenna with two-unit cells [Figure 18(d)] has exhibited  $-2^{\text{nd}}$  order (6.858 GHz) and  $-1^{\text{st}}$  order (7.31 GHz) resonances. It has been observed that the electrically small antennas exhibit low gain. Although the open-ended two-stage CRLH antenna has been greatly miniaturized, the  $-1^{\text{st}}$  order resonance of the antenna has produced an acceptable gain. The short-ended antenna (incorporated with two-unit cells) [Figure 18(e)] has also exhibited satisfactory gain. In [65], the transversal and longitudinal dimension of the antenna has been reduced by operating the antenna in LH region. The longitudinal size of the two-stage antenna has also been reduced as the periodicity of the unit cells is small as compared to the free space wavelength. The layout of the proposed antennas is presented in Figure 18.



### 4.2. Gain Enhancement

It has been observed that the incorporation of CRLH-TL metamaterials in SIW CBSAs has significantly reduced the size of antenna by enabling the antenna to resonate far below the waveguide cut-off frequency [63–65]. The application of metamaterials in antenna design has not only miniaturized the antenna structure but also enhanced the gain of the antenna. Unlike [63–65], a low impedance metamaterial design has been proposed in [66], to obtain high gain and low cross polarization (*x*-pol) level. Initially, a SIW slot antenna (SA) has been designed as a reference to verify the gain enhancement and *x*-pol minimization after employing the metamaterial to SIW SA. The SIW SA has been formed by etching an offset longitudinal slot (offset with respect to *y* axis) on a SIW cavity resonator. The reference antenna has resonated at 9.73 GHz. A cross circular loop resonator (CCLR) metamaterial has been designed, and the behaviors of effective permittivity and permeability with respect to frequency have been investigated (Figure 3 in [66]). It has been observed that the metamaterial unit cell has made the real part of effective permittivity very large and permeability very small, which is approximately near zero. Thus, the metamaterial acts as EVL (epsilon very large) and MNZ (Mu near zero) at 9.73 GHz. Hence, the intrinsic impedance of the proposed CCLR metamaterial has approached to a low value ( $\eta_r = \sqrt{\frac{\mu_r}{\epsilon_r}}$ ) and can act as a low impedance metamaterial. A low impedance metamaterial slab which consists of  $3 \times 3$  CCLR metamaterial unit cells has been placed in a superstrate to the reference SIW SA (Figure 1(b) in [66]). It has been observed in [66] that the placement of a low impedance slab at a height from magnetic source (magnetic dipole) has increased the power density as well as the broadside gain. In [66], the reference SIW SA has worked as amagnetic dipole, and the CCLR metamaterial slab (low impedance slab) has been placed at an optimum height of 3 mm. This arrangement has increased the gain of the proposed antenna by 5.6 dBi, decreased the *x*-polarization level at broadside direction by 7 dB, and increased the front to back ratio (FBR) by 9.1 dB as compared to the reference antenna (Table 1 in [66]). The layout of the proposed antenna is presented in Figure 19.



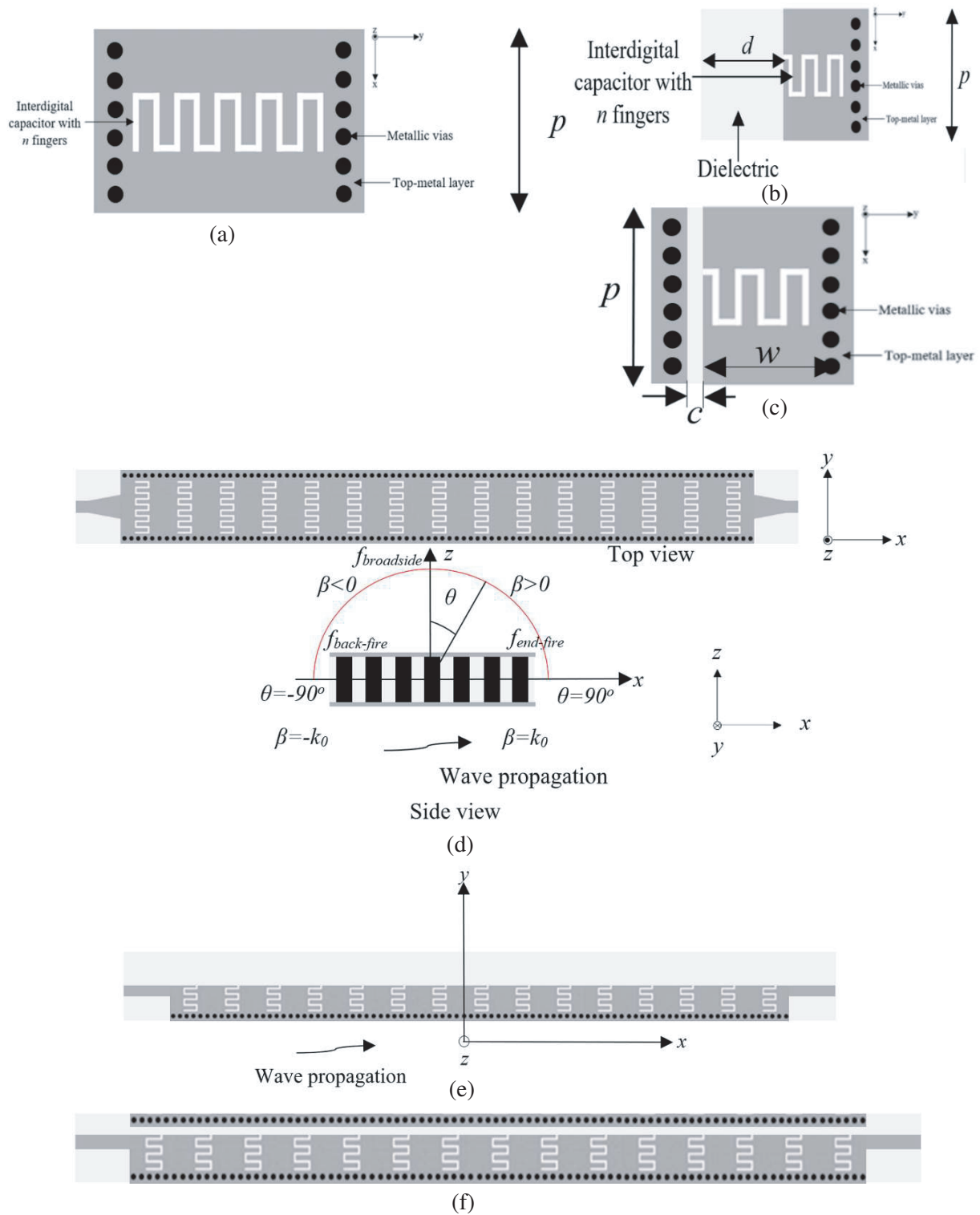
**Figure 19.** (a) Layout of the reference SIW SA, (b) CCLR metamaterial unit cell, and (c) low impedance  $3 \times 3$  metamaterial slab. Original figures are available in [66].

Different metamaterial unit cells' structures have been used in [67, 68] to enhance the gain of a magnetic dipole antenna, though the same principle of gain enhancement as described in [66]. A star-shaped, polarization-independent metamaterial unit cell has been reported in [67], which shows low

impedance characteristics (EVL and MNZ) around the antenna operating frequency. The direction of the surface current along the EM wave's polarization (Figure 3 in [67]) has made the metamaterial unit cell polarization-independent. The low impedance metamaterial slab consisting of  $3 \times 3$  metamaterial unit cells has been placed over the top of the magnetic dipole at a height of 2 mm (Figure 4(b) in [67]). The metamaterial superstrate has increased the broadside gain of the proposed antenna by 5 dBi as compared to the reference antenna (Figure 4(a) in [67]). No significant change in the cross-polarization pattern has been observed due to this gain enhancement technique. In addition to the polarization-independent, a metamaterial unit cell has been proposed in [68], which is also independent of the EM wave's incident angle. The square ring metamaterial unit cell (Figure 1 in [68]) has been designed and analyzed. Surface current distribution in the metamaterial unit cell (Figure 5 in [68]) has not been significantly changed with varying polarization and incident angles of the EM wave. Thus, the effective parameters of the metamaterial unit cell are independent of EM wave's polarization and incident angle. The square ring metamaterial unit cell has exhibited low impedance characteristics around the antenna operating frequency irrespective of various polarizations and incident angles of the EM wave. Dimension of the antenna has been reduced by eliminating the air-gap between the magnetic source and low impedance metamaterial slab. In [68], the slab consists of  $5 \times 5$  metamaterial unit cells. The influence of placing a low impedance metamaterial slab just above the magnetic source has been observed in improving the gain and front to back ratio (FBR). The broadside gain and FBR of the proposed antenna have been increased by 8.3 dBi and 9.3 dB respectively as compared to the reference antenna, whereas no significant change has been observed in the cross-polarization pattern. Another design of a metamaterial-inspired SIW leaky-wave antenna has been presented in [69] for obtaining high radiation efficiency and gain at the sub-6 GHz band. The metamaterial unit cell has comprised an interdigital capacitor and a short-circuited inductive stub. Unlike the designs reported in [66–68], this new design technique [69] has made the antenna profile low.

### 4.3. Antenna Beam Steering

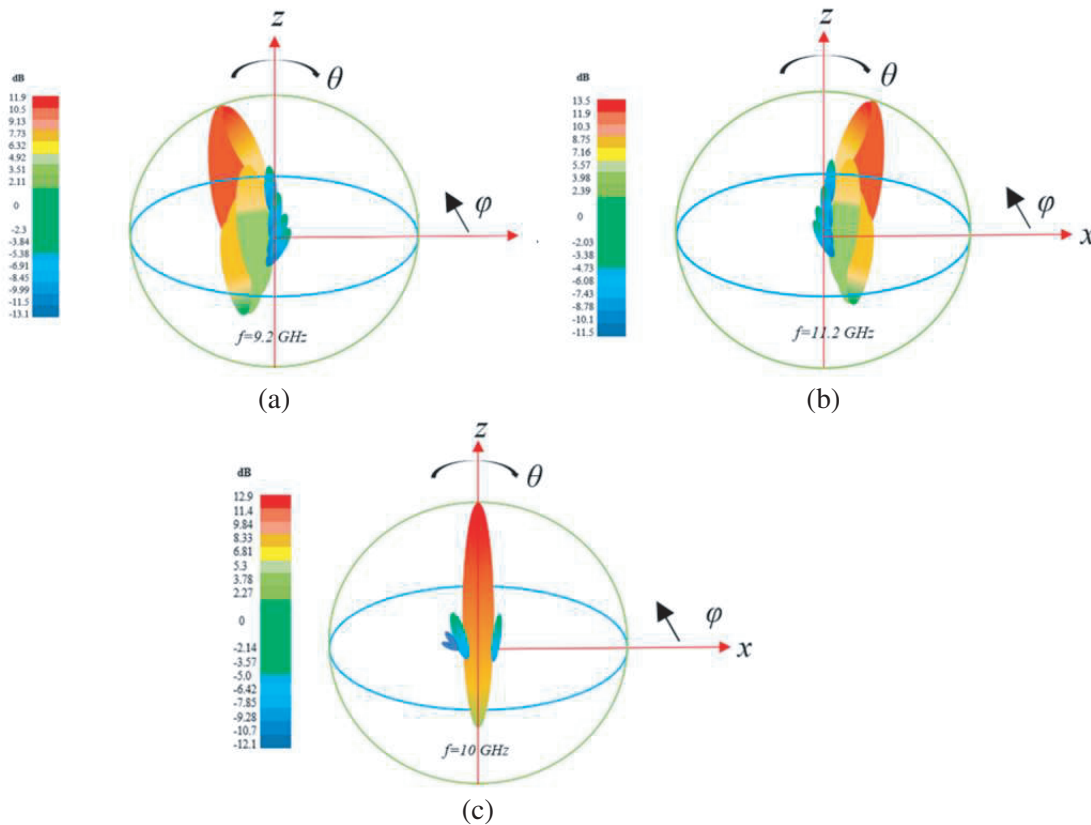
The involvement of metamaterials has been found not only in miniaturization and gain enhancement of SIW cavity-backed slot antennas but also in SIW and half mode substrate integrated waveguide (HMSIW) leaky-wave antennas in obtaining beam steering. The CRLH-TL metamaterial unit cell has been formed in the combination of SIW TL and transverse interdigital slots and presented in [70], which is quite a similar process to that has already been described in [65]. The interdigital slots on the top metallic layer of SIW and HMSIW have worked as series capacitance ( $C_L$ ) as well as radiator, and the metallic via wall of SIW/HMSIW has introduced shunt inductance ( $L_L$ ).  $C_L$  and  $L_L$  have contributed to the LH behavior. The top metal layer and ground plane of SIW/HMSIW have worked as a two-wire transmission line and introduced distributed series inductance ( $L_R$ ) and shunt capacitance ( $C_R$ ).  $L_R$  and  $C_R$  have contributed to RH behavior. Hence, the formation of a CRLH leaky-wave antenna has been confirmed. The balanced SIW and unbalanced HMSIW CRLH metamaterial unit cells [Figures 20(a) and 20(b) respectively] have been formed. The SIW CRLH leaky-wave antenna has included the periodic repetition of the 15-unit cells as observed in Figure 20(d). The SIW CRLH leaky-wave antenna has exhibited back-fire radiation when being operated in the LH region and end-fire radiation when being operated in the RH region as observed in Figures 21(a) and 21(b), respectively. The broadside radiation (Figure 21(c)) has been produced while the antenna has worked at the transition frequency (10 GHz) as the balanced SIW metamaterial unit cell has not exhibited any bandgap between the LH and RH regions (Figure 4(a) in [70]). Thus, the antenna radiation has been changed from back-fire to end-fire as the frequency increases. The SIW CRLH leaky-wave antenna has provided the beam steering of  $-70^\circ$  to  $60^\circ$  along with a maximum gain of 10.82 dBi. It is also observed from Figure 20(e) that the design of the unbalanced CRLH HMSIW leaky-wave antenna includes the periodic repetition of the 15-unit cells. Although the radiation of the unbalanced CRLH HMSIW leaky-wave antenna has been changed from back-fire to end-fire with increasing frequency, it has not generated the broadside radiation as observed in Figure 22(a). The presence of the bandgap between the LH and RH regions of the unbalanced metamaterial unit cell (Figure 4(c) in [70]) has eliminated the possibility of having a balanced point, and it is the reason for not attaining broadside radiation. The approximate beam steering of  $-75^\circ$  to  $35^\circ$  has been obtained. Some more investigations have also been carried out by incorporating interdigital slots on the bottom metallic layer of the SIW CRLH leaky-wave antenna



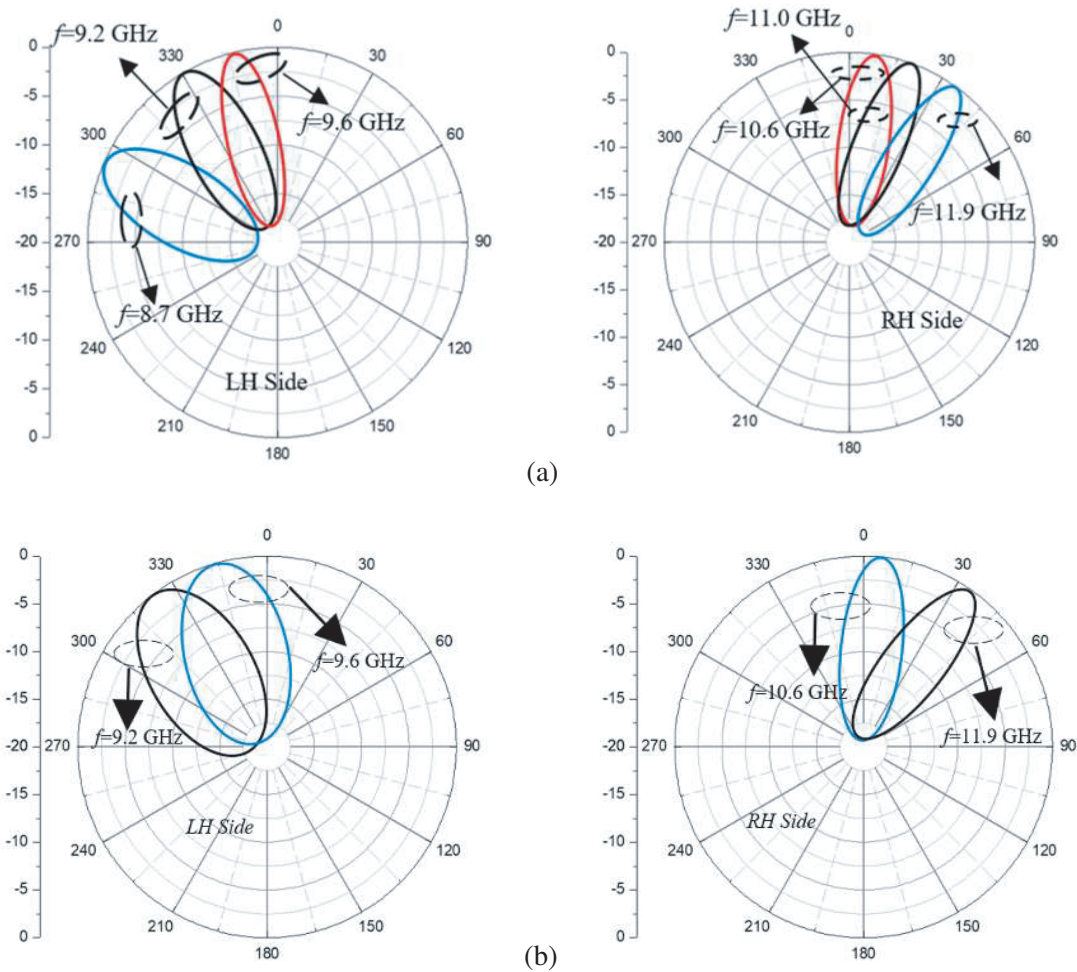
**Figure 20.** Layout of the proposed antennas: (a) Balanced SIW CRLH metamaterial unit cell, (b) unbalanced HMSIW CRLH unit cell, (c) modified unbalanced HMSIW CRLH unit cell, (d) SIW CRLH leaky-wave antenna, (e) HMSIW CRLH leaky-wave antenna, and (f) modified HMSIW CRLH leaky-wave antenna. Original figures are available in [70].

(Figure 1(b) in [70]) as well as by modifying the design of the HMSIW leaky-wave antenna. To mitigate the leakage loss from the open boundary of the HMSIW, another metallic via wall covered with a strip has been placed beside the HMSIW's open boundary. It completes the formation of the modified HMSIW CRLH metamaterial unit cell, and the structure has been reported in Figure 20(c). Like HMSIW CRLH leaky-wave antenna, the modified HMSIW CRLH leaky-wave antenna has also included 15-unit cells as observed in Figure 20(f). The radiation properties of the modified HMSIW CRLH leaky-wave antenna are reported in Figure 22(b), and it has been observed that the incorporation of the modification in the HMSIW CRLH metamaterial unit cell's structure has not affected the beam steering capability of the modified HMSIW CRLH leaky-wave antenna. The radiation properties reported in this article carry the conceptual information regarding the beam steering characteristics of the metamaterial-based antennas for the readers' easy understanding. The original radiation characteristics have been reported in [70].

A novel CRLH metamaterial unit cell has been proposed in [71], which consists of two adjacent interdigital slots with different periodicities. The design of the metamaterial unit cell is presented in Figure 23(a). The interdigital slots have been etched on the top metallic layer of the SIW transmission line. The idea of incorporating two unequally periodic interdigital slots is to obtain two different CRLH bands. Both the CRLH bands are unbalanced with a large stopband. To reduce the stopband, two metallic vias have been employed between the two CRLH slots along the centerline of the unit cell. These vias have removed the stopband from the 1<sup>st</sup> CRLH band, and hence the balanced condition in the 1<sup>st</sup> CRLH band has been maintained. Although these metallic vias have a significant role in eliminating stopband in the 1<sup>st</sup> CRLH band, less effect has been observed in reducing stopband in the 2<sup>nd</sup> CRLH band. A new RH band has also been exhibited by these metallic vias. To attain a significant reduction in the stopband between the LH and RH regions of the 2<sup>nd</sup> CRLH band by preserving



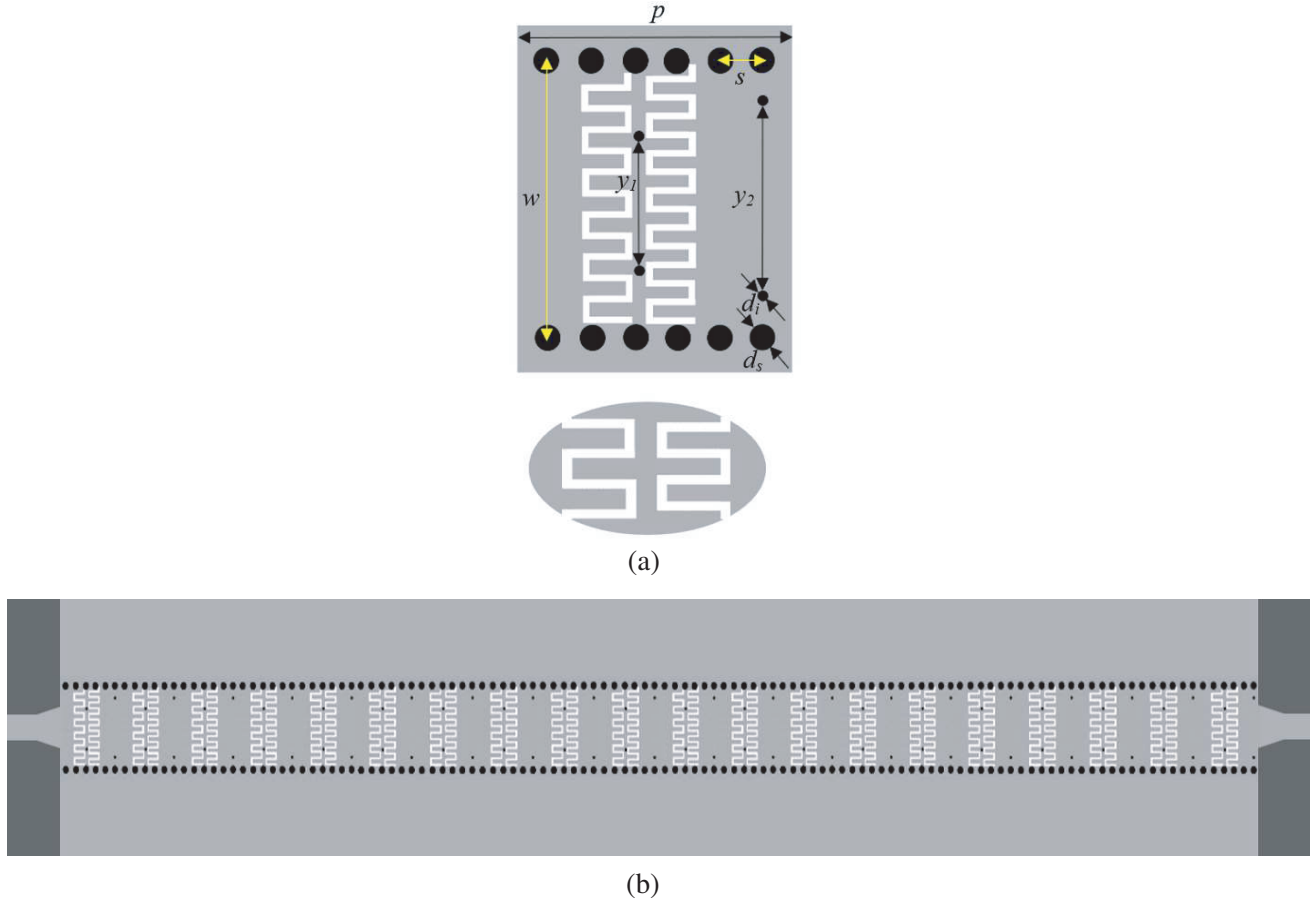
**Figure 21.** 3D Radiation patterns of balanced SIW CRLH leaky-wave antenna: (a) at 9.2 GHz (in LH region), (b) at 11.2 GHz (in RH region), and (c) broadside radiation at 10 GHz (transition frequency). Original figures are available in [70].



**Figure 22.** Normalized radiation patterns: (a) radiation patterns of unbalanced HMSIW CRLH leaky-wave antenna, and (b) radiation patterns of modified unbalanced HMSIW CRLH leaky-wave antenna. Original figures are available in [70].

the balanced condition in the 1<sup>st</sup> CRLH band, two additional metallic vias have been incorporated at the end of the unit cell. It has been observed (Figure 3 in [71]) that the 1<sup>st</sup> CRLH band ranges from 7.1 GHz to 10.75 GHz with no stopband (LH band: 7.1 GHz–8.7 GHz and RH band: 8.7 GHz–10.75 GHz, the transition frequency is 8.7 GHz), whereas the 2<sup>nd</sup> CRLH band has been extended from 15 GHz to 21.75 GHz with a stopband of 0.25 GHz (LH band: 15 GHz–19 GHz and RH band: 19.25 GHz–21.75 GHz). A stopband of 0.3 GHz (15.8 GHz to 16.1 GHz) has been spotted in the LH region at the beginning of the 2<sup>nd</sup> CRLH band (Figure 3 in [71]), and this stopband has appeared due to the spacing between the adjacent slots of each metamaterial cell. The new RH band ranges from 12.6 GHz to 13.4 GHz (Figure 3 in [71]). The CRLH leaky-wave antenna has been formed by series connection of 20-unit cells as observed in Figure 23(b). The proposed antenna is capable of beam steering through frequency scanning, ranging from  $-78^\circ$  to  $+78^\circ$  along with broadside radiation in the 1<sup>st</sup> CRLH band (the broadside radiation has been obtained at the transition frequency, i.e., 8.7 GHz),  $+22^\circ$  to  $+54^\circ$  in the new RH band, and  $-40^\circ$  to  $+20^\circ$  in the 2<sup>nd</sup> CRLH band (radiation patterns of 1<sup>st</sup> CRLH band, 2<sup>nd</sup> RH band, and 2<sup>nd</sup> CRLH band have been reported in Figures 9(a), 9(b) and 9(c) respectively in [71]). In the 2<sup>nd</sup> CRLH band, especially in the LH region the beam steering from  $-40^\circ$  to  $-33^\circ$  through the frequency scanning from 15.1 GHz to 15.8 GHz and from  $-31^\circ$  to  $-1^\circ$  by the frequency scanning from 16.1 GHz to 19 GHz has been obtained. The maximum gains of 15.3 dBi, 16.1 dBi, and 17.3 dBi have





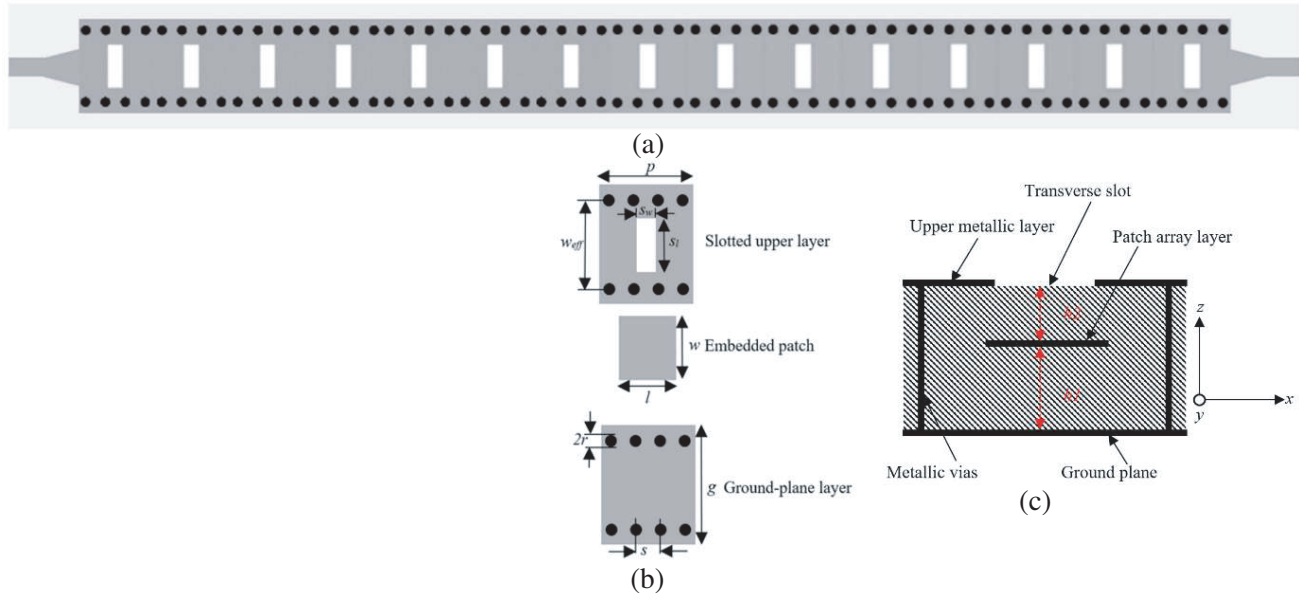
**Figure 23.** Layout of the proposed design: (a) metamaterial unit cell, and (b) leaky-wave antenna. Original figure is available in [71].

been obtained respectively in the 1<sup>st</sup> CRLH band, new RH band, and 2<sup>nd</sup> CRLH band.

Unlike the designs of SIW CRLH metamaterials described in [70, 71], a multilayer configuration has been proposed in [72], and it has brought novelty in the design of SIW CRLH metamaterial unit cells. The metamaterial unit cell has been formed by etching a transverse slot on the top metallic layer of a SIW transmission line and inserting a metallic patch in the middle layer just below the slot. The metallic patch has been placed in the SIW at a height of  $h_1 = 0.66$  mm, and the slot has been etched at a height of  $h_1 + h_2 = 0.914$  mm (the height of SIW is 0.914 mm). The proposed metamaterial unit cell has produced the LH band of 1 GHz (8 GHz to 9 GHz) and RH band of 4 GHz (9 GHz to 13 GHz) without a stopband between them (Figure 3 in [72]). Thus, the formation of balanced SIW CRLH metamaterial unit cell is confirmed. The SIW CRLH leaky-wave antenna has been formed by including 15-unit cells. It has been observed that the proposed antenna has achieved the beam steering capability ranging from  $-66^\circ$  to  $+78^\circ$ . The beam steering in the range of  $-66^\circ$  to  $0^\circ$  has been obtained in the LH region (8 GHz to 8.9 GHz), whereas the same has been obtained in the range of  $0^\circ$  to  $78^\circ$  in the RH region (9 GHz to 13 GHz) (LH and RH regions radiation patterns are presented in Figures 14(a) and 14(c) respectively in [72]). The broadside radiation has been achieved at the balanced frequency point (8.9 GHz) (Figure 14(b) in [72]). The proposed antenna has achieved the average gain of 10 dBi over the entire frequency band. The layout of the proposed antenna, metamaterial unit cell, and the cross-sectional view of the unit cell are presented in Figures 24(a), 24(b), and 24(c), respectively.

The modification to the typical form of a CRLH-TL metamaterial unit cell has been presented in [73]. The inclusion of an interdigital slot on the top metallic layer of SIW (observed in [70, 71]) has been replaced by a complementary quad spiral resonator (CQSR). Miniaturization in the design has been achieved by HMSIW technology. The combination of HMSIW-TL and CQSR has confirmed





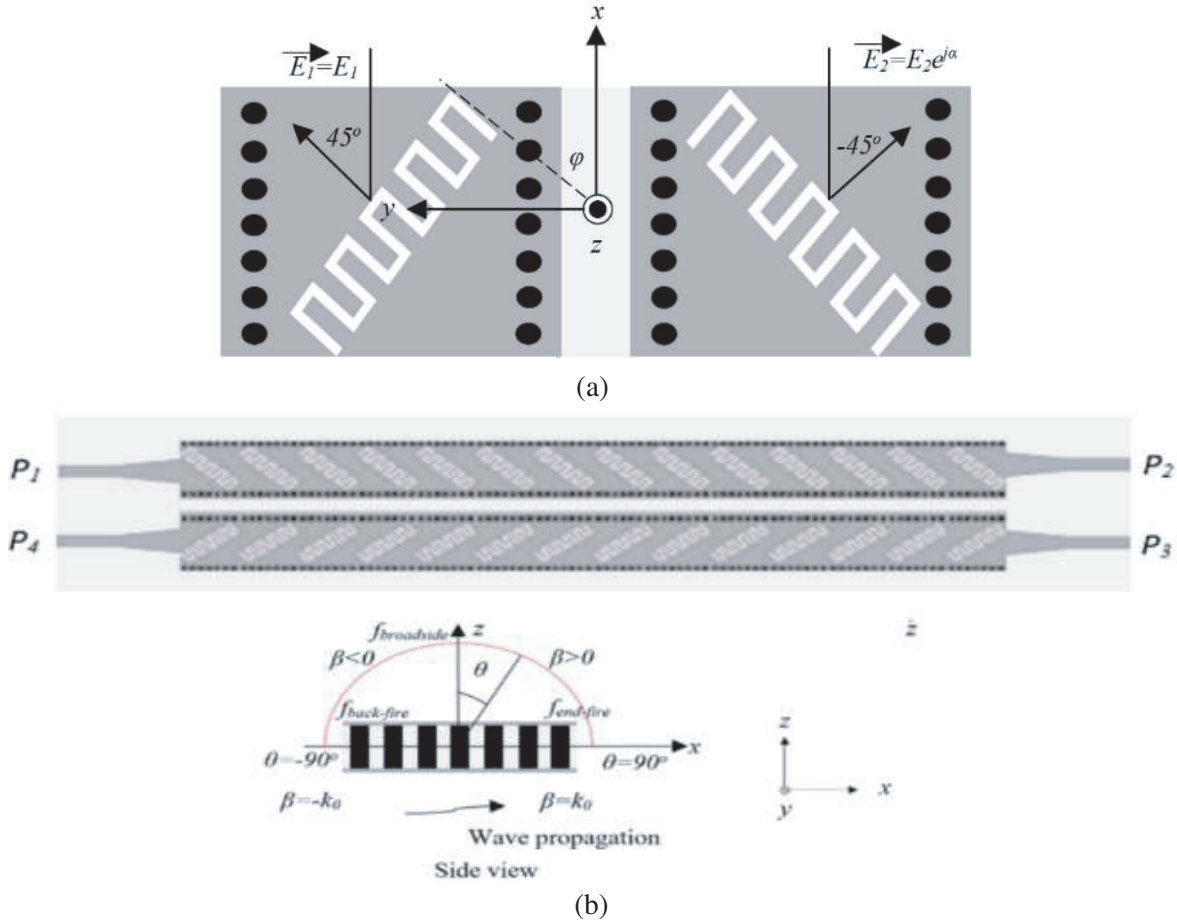
**Figure 24.** (a) Layout of the proposed SIW CRLH leaky-wave antenna, (b) design of SIW CRLH metamaterial unit cell, and (c) cross-sectional view of the metamaterial unit cell. Original figures are available in [72].

the formation of the CRLH-TL metamaterial unit cell (Figure 1 in [73]). Appropriate tuning of the distances ( $x$ -directed and  $y$ -directed) between the complementary spiral resonators has brought balanced condition in the dispersion characteristics of the metamaterial unit cell (Figure 3(a) in [73]). In [73], 8 balanced metamaterial unit cells have been cascaded to form a CRLH-TL LWA. The orientation of the spiral resonators in the metamaterial unit cell has maximized the leakage-loss and minimized the cross-coupling. The proposed antenna is capable of beam steering ( $-66^\circ$  to  $20^\circ$ ) through frequency scanning (13.5 GHz to 17.8 GHz). The proposed LWA has exhibited backward radiation in the LH region ( $13.5 \text{ GHz} \leq f < 16 \text{ GHz}$ ,  $-66^\circ \leq \theta < 0^\circ$ ), forward radiation in the RH region ( $f > 16 \text{ GHz}$ ,  $0^\circ < \theta \leq 20^\circ$ ), and broadside radiation at 16 GHz ( $\theta = 0^\circ$ ), as 16 GHz is the transition point between the LH and RH regions. Maximum gain of 16 dBi along with the radiation efficiency of 85% have been obtained by the proposed design. A transverse E-shaped slot has also been used to design the CRLH-TL LWA to obtain beam steering [74]. Instead of designing the LWA on SIW/HMSIW platform, a completely novel design approach for LWA based on the eighth mode SIW (EMSIW) technology has been proposed in [75]. The balanced metamaterial unit cell is compact in nature and has been formed by etching an interdigital capacitor slot on the top metallic layer of the tilted EMSIW (Figure 1(a) in [75]). Ten metamaterial unit cells have been cascaded to form the LWA (Figure 8(b) in [75]). The structure of the LWA is asymmetric around both the  $x$ - and  $y$ -axes. The proposed LWA has shown the beam steering capability of  $107^\circ$  ( $-64^\circ \leq \theta \leq +43^\circ$ ) through frequency scanning (9 GHz to 13.5 GHz) along with the broadside radiation at 11.5 GHz. The proposed antenna has exhibited a very high gain of 17.96 dBi. The formation of the balanced/unbalanced SIW/HMSIW CRLH-TL LWAs is not the only way to obtain beam steering. Recently, a novel approach to attaining beam steering has been reported in [76], including the mushroom-type metamaterial loading in front of a SIW aperture antenna (Figure 1 in [76]). The dispersion characteristics of the mushroom type metamaterial have exhibited an LH mode and a band-gap mode (Figure 3(a) in [76]). As described earlier, in the LH mode the antenna radiates in the back-fire direction. The EM wave propagation in the metamaterial structure is prohibited in the band-gap region. Thus, there is a possibility of the radiation in the perpendicular direction to the metamaterial structure. By using this unique property of the mushroom-type metamaterial, the beam switching between the back-fire and boresight direction has been achieved. Modified probe to SIW transition has been used not only to excite the antenna but also to enhance the impedance bandwidth. The impedance bandwidth of the SIW aperture antenna should be capable to cover both the LH band

and band-gap region of the metamaterial to obtain beam steering. In [76], the proposed SIW aperture antenna has the impedance bandwidth ranging from 13.3 GHz to 16.7 GHz, whereas the mushroom-type metamaterial has exhibited the LH behavior in the band 12.6 GHz to 15.1 GHz and band-gap mode beyond the 15.1 GHz. The radiation performance analysis (Figure 5 in [76]) of the proposed antenna has revealed that the back-fire radiation has been obtained at 13.3 GHz (LH region), and the radiation perpendicular to the plane of the metamaterial (boresight direction) has been achieved at 16.7 GHz (band-gap region). It has also been observed that at the transition of these two modes (15 GHz), the direction of the maximum radiation is in between the boresight and back-fire direction.

#### 4.4. Polarization Flexibility

A SIW based CRLH leaky-wave polarization flexible antenna has been reported in [77]. Like the designs presented in [70, 71], the formation of a SIW CRLH metamaterial unit cell in [77] has also been accomplished in the combination of an interdigital slot and a SIW transmission line. The interdigital slot has been not only worked as the series capacitance but also acted as a radiator, and hence the formation of a SIW CRLH leaky-wave antenna has confirmed. Unlike [70, 71], here the interdigital slot has been etched on the top metallic layer of SIW transmission line at an angle of  $45^\circ$  with respect to the direction of wave propagation through the waveguide. Quite a different approach has been adopted in formation of the antenna unit cell. The antenna unit cell consists of two symmetrical leaky-wave transmission lines, which have been placed side by side and separated by an optimum distance to improve the isolation. The structure of the antenna unit cell is presented in Figure 25(a). The




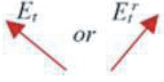

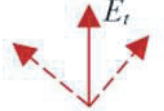
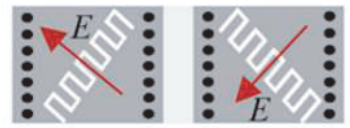
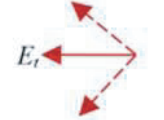
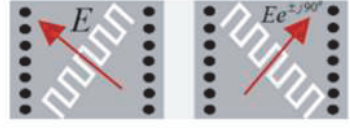
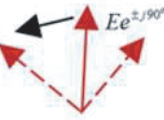
**Figure 25.** Layout of the antenna: (a) SIW CRLH leaky-wave antenna unit cell, and (b) proposed leaky-wave antenna. Original figures are available in [77].

proposed antenna consists of four ports as well as includes the periodical repetition of 14 antenna unit cells (Figure 25(b)). The individual excitation to the port 1 and port 4 has exhibited two orthogonally polarized waves. Typically, the resultant electric field is the vector addition of the fields radiated by the two leaky-wave TLs. The left side leaky-wave TL has generated a linearly polarized wave at  $\varphi = +45^\circ$  direction (excitation to the port 1 only), whereas the right side leaky-wave TL has produced a linearly polarized wave at  $\varphi = -45^\circ$  direction (excitation to the port 2 only). The simultaneous excitation to ports 1 and 4 with equal magnitude and in-phase signals has generated an  $X$ -directed linearly polarized wave, whereas the excitation with equal magnitude and out of phase signals has generated a  $Y$ -directed linearly polarized wave. The right-handed and left-handed circular polarizations (RHCP/LHCP) have been obtained by simultaneous excitation with the signals of equal magnitude and  $\pm 90^\circ$  phase difference to the antenna ports 1 and 4. The mechanism of obtaining polarization flexibility has been presented in detail in Table 2. It has been observed that the etching of tilted interdigital slots on the top metallic layer of SIW TL has brought the polarization flexibility in the proposed antenna design. Rat-race coupler is a 4 ports device. Typically,  $180^\circ$  and  $0^\circ$  phase difference can be obtained between the output ports of the coupler (ports 2 and 3) while individually the coupler's input ports 1 and 4 are respectively excited. Similar to a rate-race coupler, an HMSIW 3 dB directional coupler is also a 4 ports device, and  $\pm 90^\circ$  phase differences can be obtained between the output ports (ports 2 and 3) of the coupler while individual excitations are given to the coupler's input ports 1 and 4, respectively. The rat-race coupler (Figure 6(b) in [77]) and HMSIW 3 dB directional coupler (Figure 7(b) in [77]) have been designed and fabricated. Typically, these couplers are capable to provide simultaneous excitation to the antenna's input ports 1 and 4, along with required phase differences between the excitation signals for generating linearly polarized waves as well as RCHP/LHCP waves. In the measurement process of the radiation characteristics of the proposed antenna, the rat-race coupler has been cascaded to the SIW CRLH leaky-wave antenna (Figure 14 in [77]) in obtaining  $X$ -directed/ $Y$ -directed linearly polarized wave, whereas the HMSIW 3 dB directional coupler has been cascaded to the antenna (Figure 20 in [77]) for achieving RHCP/LHCP waves. The  $X$ -directed and  $Y$ -directed linearly polarized waves have been obtained by providing individual excitation to the rate-race coupler's input ports 4 and 1, respectively. The RHCP and LHCP waves have been achieved with the individual excitation to the HMSIW 3 dB coupler's input ports 1 and 4, respectively. The back-fire to end-fire beam steering has been achieved for each polarization through frequency scanning by the proposed antenna. Backward radiation has been achieved while the antenna operates in the LH frequency region, and forward radiation has been achieved while the antenna operates in the RH frequency region. The antenna has exhibited broadside radiation at the transition frequency. The axial ratio is well below 3 dB for RHCP/LHCP at LH and RH regions as well as at transition frequency. The proposed antenna has exhibited highly directive radiation patterns with minimized cross polarization level.

#### 4.5. Isolation Improvement

Isolation enhancement between the individual antenna elements of multiple-input multiple-output (MIMO) antennas can also be obtained by utilizing metamaterial. A four element SIW CBSA has been designed for MIMO application in [78]. The layout of the MIMO antenna is presented in Figures 26(f)-(ii). Although orthogonal arrangement of the antenna elements in the proposed MIMO antenna has significantly maximized the isolation level between the antenna elements, but the isolation between the parallelly positioned antenna elements in the same MIMO antenna has not been significantly improved. The inter-element isolation between the orthogonally arranged antenna elements (Ant1/Ant2, Ant2/Ant3, Ant3/Ant4, and Ant4/Ant1) is below  $-40$  dB, whereas the isolation is below  $-20$  dB between the parallelly positioned antenna elements (Ant1/Ant3 and Ant2/Ant4). It has been observed that the isolation between the parallelly positioned antenna elements (diagonal elements) is quite low. To improve the isolation between these diagonal elements, a cross-shaped double-layer mushroom wall has been placed [Figures 26(f)-(i) and 26(f)-(ii)], and it has provided a symmetrical partition between the four antenna elements. The double layer mushroom cell has been formed by sandwiching a ground plane between two dielectric substrates and etching two metallic patches of equal dimensions on the top of the upper dielectric layer and bottom of the lower dielectric layer [Figures 26(a), 26(b) and 26(c)]. The connection of the metallic patches to the sandwiched ground plane has been accomplished by inserting a metallic post from top to bottom layer through the ground plane. The crossed-wall structure has been

**Table 2.** Polarization flexibility mechanism. Original table is available in [77].

Polarization State	Excitations	Electric Field Distribution	Working Scheme
$\varphi = \pm 45^\circ$ Linear Polarization	$E_1 \neq 0, E_2 = 0$ or $E_1 = 0, E_2 \neq 0$		
X-Directed Linear Polarization	$E_1 = E_2$ and $\alpha = 0^\circ$		
Y-Directed Linear Polarization	$E_1 = E_2$ and $\alpha = 180^\circ$		
Circular Polarization (RHCP & LHCP)	$E_1 = E_2$ and $\alpha = \pm 90^\circ$		

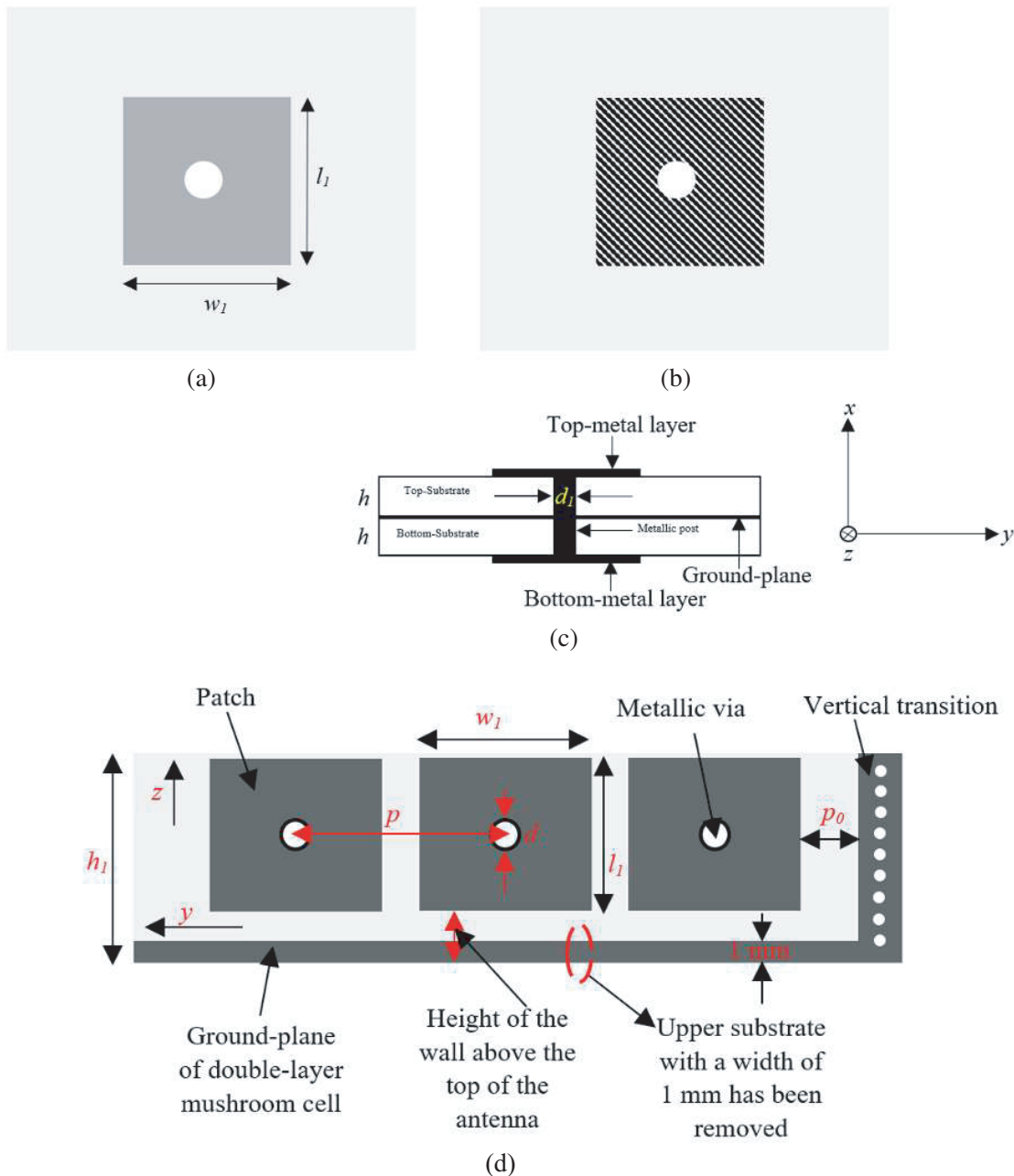
created by four sections of double-layer mushroom walls, which have been connected to each other by a vertical transition as observed in Figures 26(f)-(i). It has been observed from Figures 26(e)-(ii) that the ground plane of the four mushroom walls has been connected together at the vertical transition by four rows of metallic vias. The side view and perspective view of the vertical transition are respectively presented in Figures 26(e)-(i) and 26(e)-(iii). To connect the ground plane of the mushroom wall (the ground plane is sandwiched between the upper and lower dielectric layers) to the ground of the antenna elements, a certain portion of a width of 1 mm from the upper dielectric layer of the metamaterial wall has been removed [notified in Figure 26(d)]. The double-layer mushroom cell has exhibited a bandgap of 0.4 GHz (2.4 GHz–2.8 GHz) to forbid the surface wave excitations (Figure 11 in [78]). The optimum design of the mushroom wall (1 unit) has included 1 row and 3 columns of the mushroom cells, depending upon the center operating frequency (2.42 GHz) and height of the antenna as observed in Figure 26(d). The height of the double-layer mushroom wall above the top of the antenna [mentioned in Figure 26(d)] is a crucial parameter in improving isolation between the antenna elements. The possibility of TM mode surface wave coupling to the antenna 2, while the antenna 1 has radiated the field, has been suppressed by increasing the height of the mushroom wall above the top of the antenna, as the TM mode surface wave propagates along the  $z$ -axis and crosses over the mushroom wall. Unlike the TM mode, the TE mode surface wave propagates along the  $y$ -axis or  $x$ -axis of the mushroom wall around antenna 1 for coupling to the other antenna elements. It has been reflected by the metallic vias of the vertical transition. It has been observed that the isolation between the parallel antenna elements has been increased by 16 dB, and the same is well below  $-42$  dB between any antenna elements. Unlike the designs of metamaterial unit cells presented in [70–72], to obtain desired performance based upon the requirement (isolation enhancement), a completely different metamaterial structure has been proposed in [78]. Thus, it can be stated that the flexibility in metamaterial applications in SIW-based antenna technology as per the specific requirement can be achieved by varying the design topology of metamaterial unit cells.

Another example of suppressing mutual coupling between the antenna elements by utilizing SIW

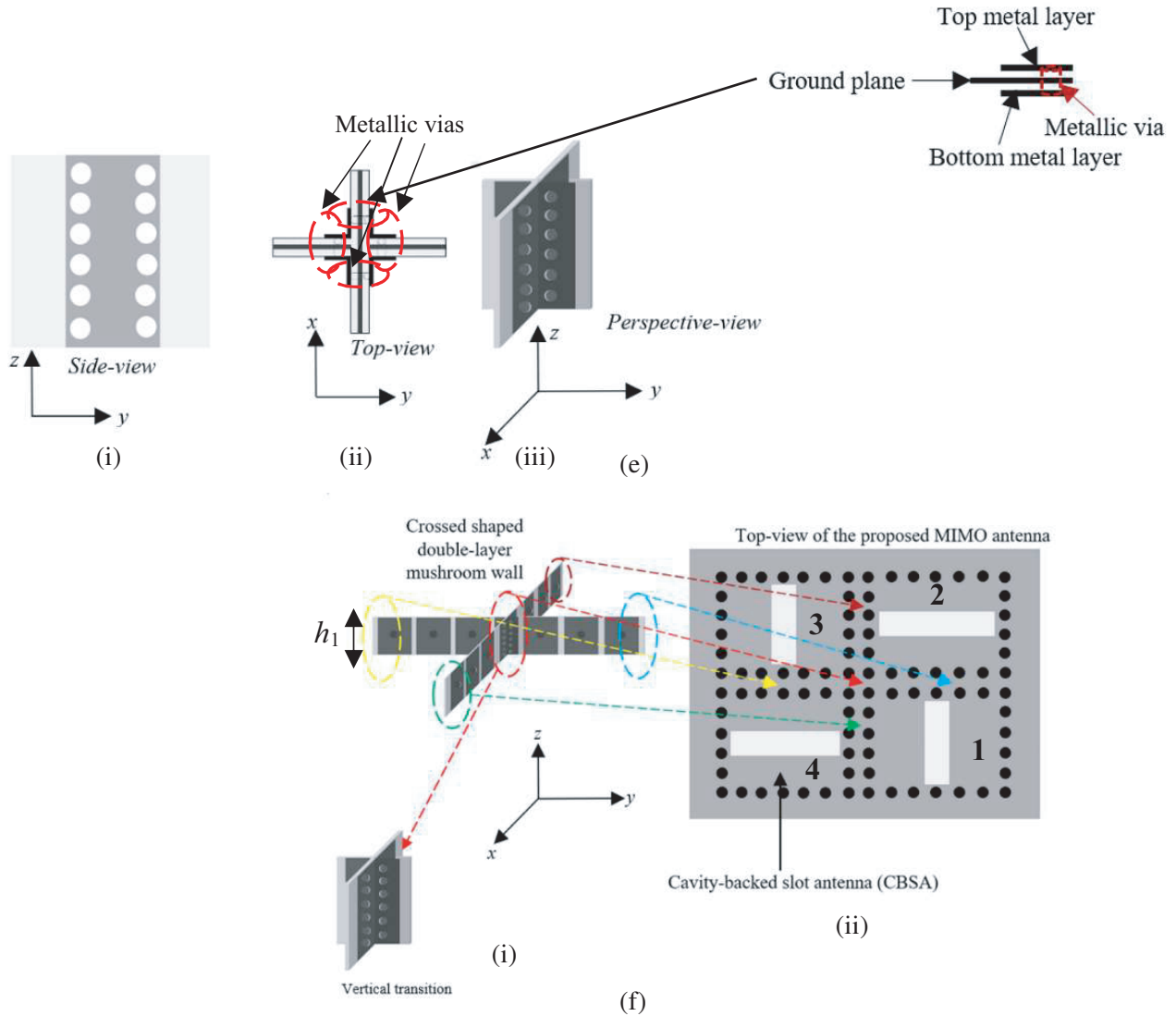
based metamaterial shield has been found in [74]. The metamaterial shield consists of tapered transverse slots, and it has been placed between the two SIW CRLH-TL LWAs (Figure 4 in [74]). This metamaterial shield has suppressed the surface wave, so as to increase the isolation between the two LWAs (Figure 5 in [74]). The insertion of the metamaterial shield has significantly improved the cross-polarization pattern, radiation gain, and efficiency of the antenna over the entire operating band. In comparison to [78], a more compact structure has been proposed in [74] to enhance the isolation between the LWAs. Some more examples of minimizing mutual coupling in MIMO antennas have been reported in [79–81].

#### 4.6. Enhancement of Impedance Bandwidth

The application of metamaterial has also been explored by the researchers in broadening the bandwidth of SIW based antennas. In [82], initially a SIW *H*-plane horn antenna has been designed, and its





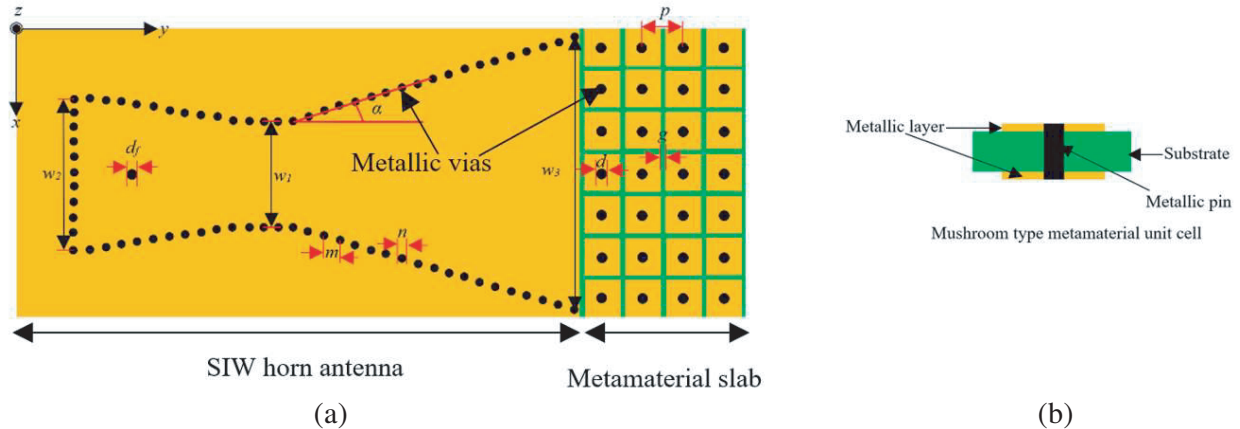


**Figure 26.** Layout of the Double-layer mushroom unit cell: (a) top view, (b) bottom view, (c) cross-sectional view, (d) structure of one-unit mushroom wall, (e) layout of vertical transition, (f) layout of the proposed MIMO antenna. (Arrows represent exact placement of the cross-shaped mushroom wall in the MIMO antenna). Original figures are available in [78].

performance has been investigated. It has been observed that the antenna has exhibited very narrow bandwidth (Figure 2 in [82]). The loading of mushroom type metamaterial unit cells in front of horn aperture has enlarged the impedance bandwidth of the SIW  $H$ -plane horn antenna beyond 10% (14.4 GHz to 16 GHz) (observed in Figure 2 in [82]). Thus, the metamaterial can be considered as the impedance transformer. The mushroom type metamaterial unit cell has been formed by etching metallic patches on either side of the substrate and shorting these patches by inserting a metallic post from the top metallic patch to the bottom patch through the substrate as observed in Figure 27(b). A comparative analysis of the input impedances of the SIW  $H$ -plane horn antenna with and without metamaterial loading has been carried out (presented in Figure 3 in [82]). It has been observed that the real part of the input impedance of the conventional horn antenna is near the characteristics impedance of the SIW ( $Z_{SIW}$ ) only at 14.7 GHz, whereas the real part of the input impedance of the metamaterial loaded SIW horn antenna is closer to the  $Z_{SIW}$  over wide frequency bands (14 GHz–17 GHz). On a closer look at the metamaterial slab, it is evident that the equivalent circuit of the mushroom type



metamaterial cell includes capacitance ( $C$ ) and inductance ( $L$ ). The gap ( $g$ ) between the patches constitutes the capacitance  $C$ , whereas the inductance  $L$  comes due to the metallic via. The values of  $C$  and  $L$  can be changed by varying parameters  $g$  and  $d$ , respectively, so as the attainment of varying characteristics impedance of the equivalent circuit. Thus, it is possible to obtain impedance matching at a different frequency. The rigorous investigations have been carried out by varying the parameters such as  $p$  (periodicity of the metamaterial unit cells),  $d$ , and  $g$ , and it has been observed that the operating band of the antenna is enhanced either by increasing  $d$  or  $g$ , while rest of the parameters are kept unchanged. The characteristics of mushroom type metamaterial unit cell have been investigated, and it has been observed that the LH mode has been supported by the metamaterial unit cell over the frequency band of 13.8 GHz to 16.3 GHz. Due to the operation of metamaterial unit cell in LH region over the antenna working bandwidth, the SIW  $H$ -plane horn antenna has exhibited backward end-fire radiation. The antenna gains with a variation in the range of 6.3 dBi to 8.1 dBi have been obtained over the frequency band of 14.4 GHz to 16 GHz. The formation of SIW  $H$ -plane horn antenna and antenna arrays with metamaterial loading in front of horn apertures has exhibited a wider bandwidth of more than 10% despite inclusion of thin substrate ( $0.05\lambda_0$ ) in the antenna design. The layout of the SIW  $H$ -plane horn antenna with metamaterial loading is presented in Figure 27(a).



**Figure 27.** (a) Layout of the proposed SIW  $H$ -plane horn antenna with metamaterial loading, and (b) layout of the metamaterial unit cell. Original figures are available in [82].

Another application of the metamaterial in enhancing the impedance bandwidth of the SIW slot antenna for millimeter-wave application (Ka-band) has been observed in [83]. Initially, the formation of the antenna has been accomplished by incorporating a roman “I” shaped slot on the top metallic layer of the SIW cavity (Figure 2 in [83]). The antenna has exhibited an impedance bandwidth of 1.1 GHz, ranging from 27.6 GHz to 28.7 GHz (Figure 3(a) in [83]). Further, the bandwidth broadening has been achieved by integrating the CRLH-TL metamaterial unit cell on either side of the antenna feed line (Figure 5 in [83]). The metamaterial unit cell has comprised three-ring split-ring resonators as observed in Figure 4 in [83]. The influence of inserting metamaterial in antenna design has been clearly observed in the antenna’s impedance bandwidth which has been increased to 3.7 GHz (Figure 6 in [83]). Apart from the above-mentioned works [82, 83], the application of metamaterial has also been found in broadening the impedance bandwidth of open-ended SIW antenna. A CRLH-TL metamaterial-based SIW open-ended antenna has been presented in [84]. The formation of the CRLH-TL metamaterial has been accomplished by etching two longitudinal inter-digital capacitor slots on the top metallic layer, near both the side walls of the SIW. The bandwidth enhancement has been obtained by etching two unequal “U” shaped slots on the antenna’s ground plane (Figure 1 in [84]). Merging resonances due to the open-ended SIW cavity and “U” shaped slots has enhanced the impedance bandwidth of the proposed antenna. The antenna has exhibited impedance bandwidth of 16.74%, ranging from 11.88 GHz to 14.05 GHz (Figure 7 in [84]). The insertion of unequal “U” shaped slots on the antenna’s ground

plane has not only enhanced the impedance bandwidth but also brought miniaturization to the design. It has been clearly observed in Figure 5 [84] that the insertion of unequal “U” shaped slots has lowered the antenna resonance frequency, and miniaturization of 23.5% has been achieved as compared to the conventional SIW antenna. The conventional SIW antenna has been presented in Figure 4(b) in [84].

#### 4.7. Gain Enhancement of SIW and HMSIW *H*-Plane Horn Antennas

In another approach [85], metamaterial cells (capacitively loaded loop: CLL) have been etched in the flaring of SIW and HMSIW *H*-plane horn antenna to enhance the gain. The layout of a CLL unit and CLL loaded SIW and HMSIW *H*-plane horn antennas are presented in Figures 28(a), 28(b), and 28(c) respectively. The CLL has exhibited negative permittivity and permeability over the operating bandwidth of conventional SIW *H*-plane horn antenna (Figure 13 in [85]), and hence the formation of LHM has been confirmed. It is evident from Figure 28(d) that the etching of capacitively loaded loop in horn’s flaring has led to concentration of the surface current at the middle of the modified horn’s aperture as compared to the conventional SIW *H*-plane horn antenna. In conventional SIW *H*-plane horn antenna, the current distribution can be observed throughout the whole aperture. Thus, the CLL (in [85] the CLL has worked as LHM) has worked as the focusing device and increased the gain of the antenna. The comparative study of the antenna gains with and without metamaterial cells is reported in Table 3.

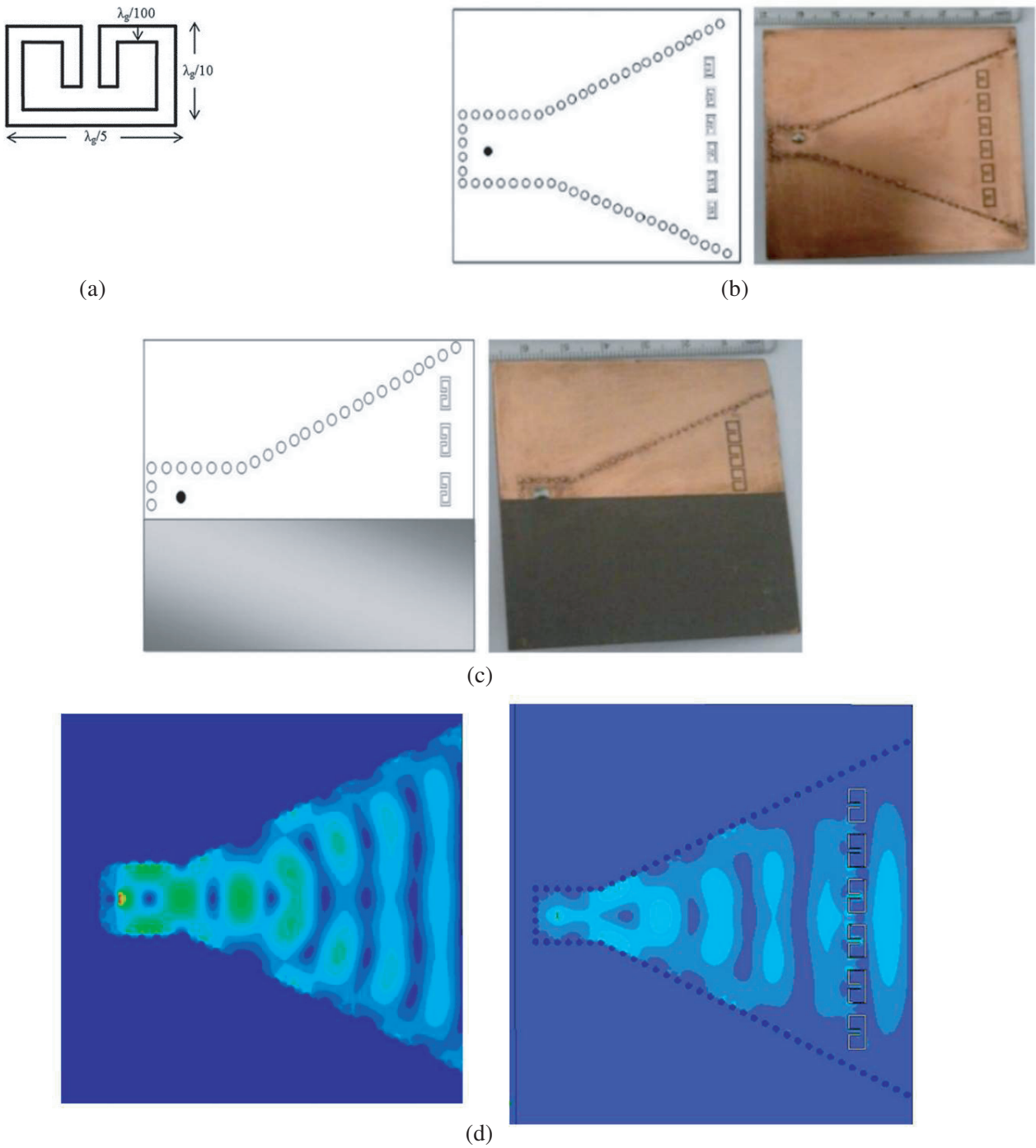
**Table 3.** Comparative study of antenna gains. Adopted from [85].

Types of antennas	Gain in dB	
	Calculated	Measured
SIW horn antenna without metamaterial	4	3.82
SIW horn antenna with metamaterial	94	7.20
HMSIW horn antenna without metamaterial	4	3.82
HMSIW horn antenna with metamaterial	6.5	5.57

The application of the metamaterial has also been found in amplifying the gain of the substrate integrated cavity (SIC) backed dipole antenna array. In [86], initially, a substrate integrated cavity-based power splitter has been designed (Figure 1 in [86]). Semi-triangular shaped dipole antenna elements have been connected to the output ports of the power splitter to complete the structure of the antenna array (Figure 4 in [86]). Grounded coplanar waveguide (GCPW) transition has been used to connect the microstrip feed line of the dipole antenna to the output ports of the SIC power splitter. Epsilon near zero (ENZ) material has been used to enhance the gain. The  $3 \times 2$  ENZ metamaterial slab has been kept in front of each dipole antenna, and it has been placed perpendicularly to the plane (*xy*-plane) of the antenna and SIC power splitter (Figure 8 in [86]). The surface current distribution is symmetrical in the metamaterial unit cell. The implementation of the metamaterial slab in the antenna design has guided the EM field uniformly along the *z*-direction. Thus, the attainment of the gain enhancement has been possible. The gain of the proposed antenna has been improved by 5 dBi over the entire working band as compared to the dipole antenna array without metamaterial slabs.

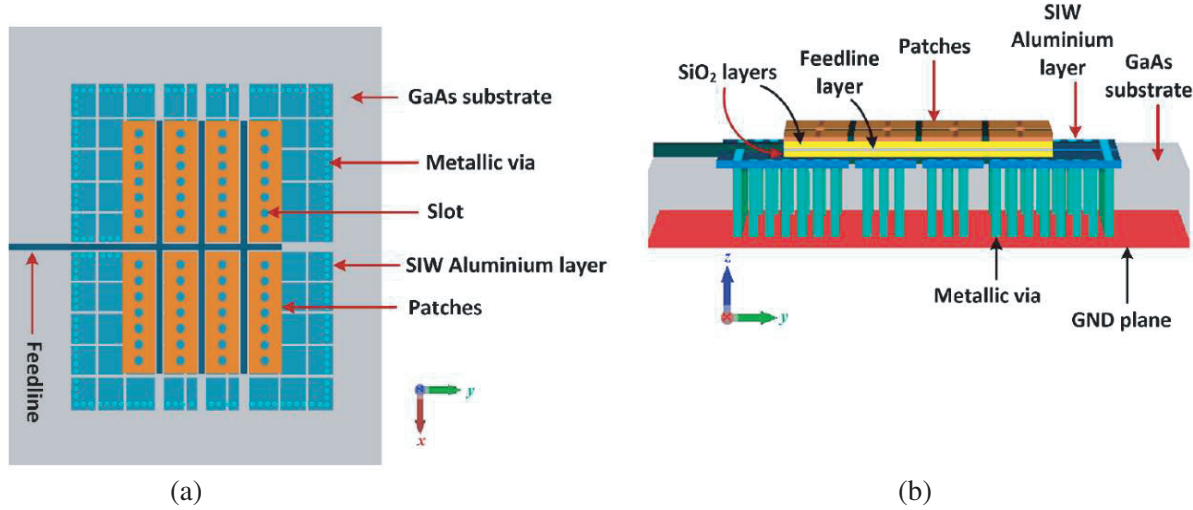
#### 4.8. Performance Improvement of SIW Based On-Chip Antennas in THz Frequency Band

A literature survey on on-chip antennas based on metamaterial, metasurface, and SIW has been carried out in [87]. The designs of metamaterial-inspired SIW based on-chip antennas have been presented in [88–91]. Very small size of the antenna in THz frequency limits the bandwidth, gain, and efficiency of the antenna. Combining two techniques namely SIW and metasurface in [88] enhances the performance of the on-chip antenna. Seven stacked layers of Cu-SiO<sub>2</sub>-Cu-SiO<sub>2</sub>-Al-GaAs-Cu have been used to realize the on-chip antenna. A  $2 \times 4$  array of rectangular radiating patches has been incorporated on the top Cu layer [Figure 29(a)]. Etching of circular slots of subwavelength diameter in the rectangular patches



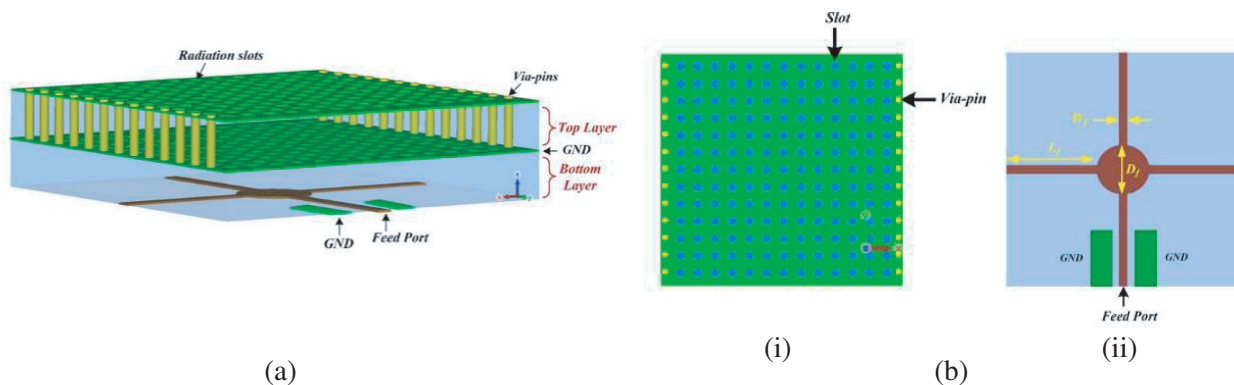
**Figure 28.** (a) Layout of metamaterial unit cell, and (b) layout and fabricated structure of SIW *H*-plane horn antenna with metamaterial loading. (c) Layout and fabricated structure of the HMSIW *H*-plane horn antenna with metamaterial loading, and (d) current distribution in SIW *H*-plane horn antenna with and without metamaterial loading. Adopted from [85].

has increased the effective aperture area as well as converted the patches into metasurface. It has been observed from Figure 29(b) that the antenna has been excited by CPW feed, which has been sandwiched between the two  $\text{SiO}_2$  substrates below the top Cu layer. The metasurface layer along with the sandwiched CPW line has been placed upon a SIW cavity [Figure 29(b)]. The formation of cavity



**Figure 29.** Layout of Antenna on Chip (AOC): (a) top view, and (b) side view. Adopted from [88].

has involved the insertion of metallic pins from Al (Aluminum) layer to Cu ground plane through the  $100\ \mu\text{m}$  GaAs substrate [Figure 29(b)]. The inclusion of SIW in the antenna design has significantly minimized the surface wave propagation and radiation loss. The Al layer consists of several Al patches along with narrow slots between them as observed in Figure 29(a), and this layer has worked as a perfectly reflecting surface. The incident EM wave has penetrated through these gaps in the Al layer and reflected by the ground plane with zero phase shift. Thus, the reflected waves from the ground plane, Al layer, and surface of the Cu patches are in phase and have increased the antenna directivity. The thickness of the GaAs substrate has played a major role in providing in-phase ground plane reflected wave. Finally, the proposed antenna has exhibited an impedance bandwidth of 50 GHz ranging from 0.45 THz to 0.5 THz and a maximum radiation gain of 7.4 dBi. As discussed earlier, the demerits of the on-chip antenna are low impedance bandwidth and radiation efficiency, which have resulted from the small aperture size of the antenna and surface wave excitations. Similar to [88], the combination of metasurface and SIW has been proposed in [89] to overcome these limitations. The antenna has been realized with the five stacked layers of metal-silicon-metal-silicon-metal. The SIW cavity has been engraved with circular slots of subwavelength diameter on its top and bottom metal layers [Figure 30(a)]. Figure 30(b)-(i) present the top view of the proposed SIW cavity. Etching of circular slots has enlarged the effective aperture of the antenna as well as confirmed the formation of the Metasurface. A feeding network along with CPW excitation has been designed to stimulate the antenna [Figure 30(b)-(ii)].



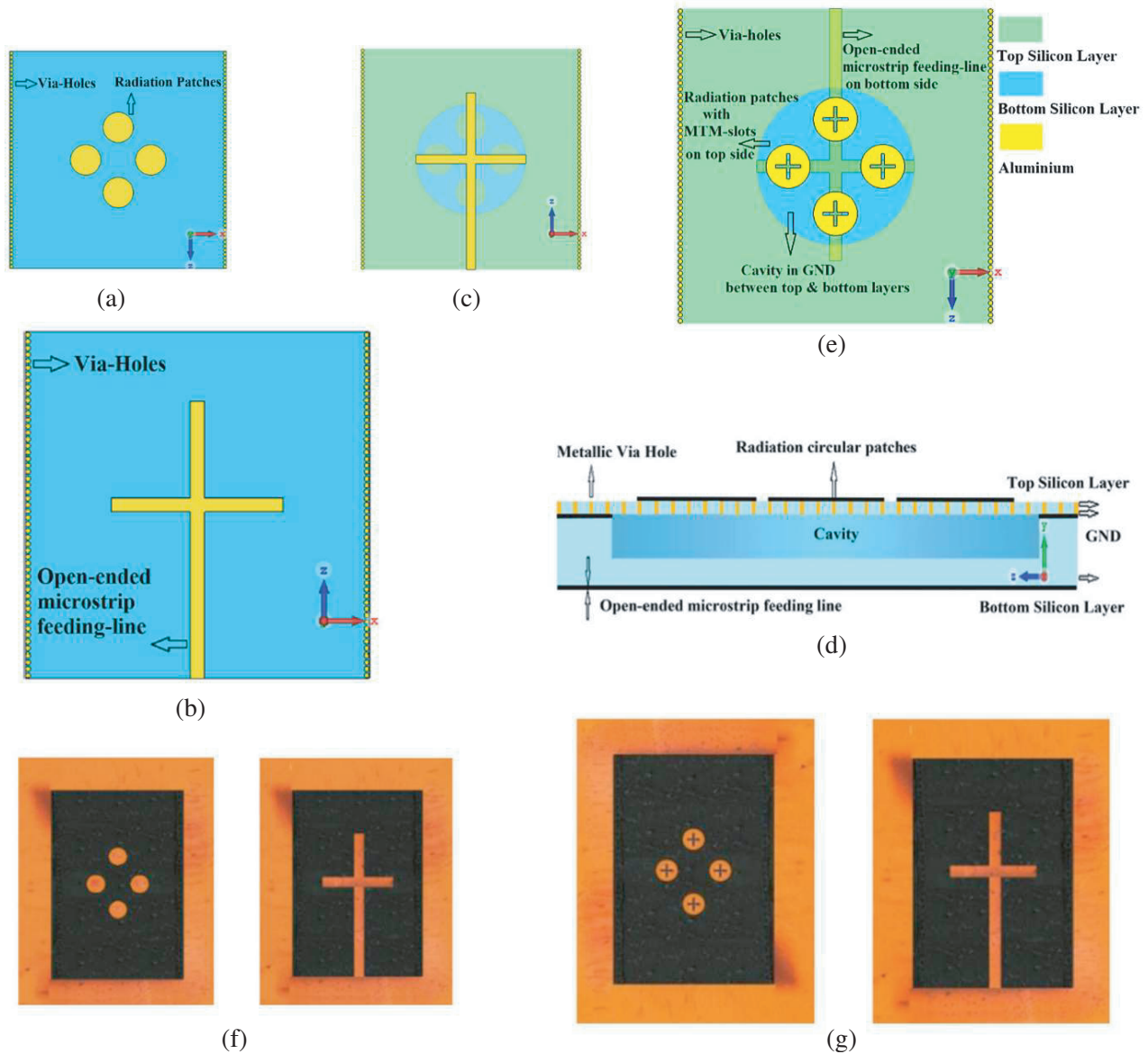
**Figure 30.** Layout of Antenna on Chip (AOC): (a) 3D view, (b)-(i) top view, and (b)-(ii) feedline structure. Adopted from [89].

The feeding network has been placed on the bottom side of the lower silicon substrate, and this silicon substrate has been positioned beneath the SIW cavity as observed in Figure 30(a). The feeding network has three branches of open-ended microstrip line, and the branches have met at the circular-shaped junction [Figure 30(b)-(ii)]. The diameter of the circular junction has played a key role in the impedance matching of the feeding network to the antenna. Excitation to the CPW feed has delivered the EM energy to all the feeding network branches. This EM energy has been coupled to the radiating slots on the top metallic layer of the SIW cavity through the two silicon substrates and the circular slots on the bottom layer of the SIW cavity. The proposed design has exhibited the impedance bandwidth of 20 GHz ranging from 0.2 THz to 0.22 THz, as well as a maximum gain of 9 dBi at 0.21 THz. Another design of metamaterial and SIW-based on-chip antenna has been reported in [90]. A 0.5  $\mu\text{m}$  GaAs substrate has been used to implement the on-chip antenna. The proposed antenna has produced an impedance bandwidth of 10 GHz ranging from 0.3 THz to 0.31 THz and a maximum gain of 1.75 dBi at 0.305 THz. Another example of performance improvement of the on-chip antenna has been found in [91]. Similar to the previously reported works [88–90], the combination of metamaterial and SIW has been in effect for enhancing the on-chip antenna's performance. The layouts of reference on-chip antenna and metamaterial-inspired on-chip antenna have been presented respectively in Figures 31(a)-(d) and 31(e). A SIW cavity has been formed by inserting metallic pins from the top metallic layer to the ground plane through a silicon substrate. Some of the metallization has been removed from the middle of the top metallic layer by keeping intact the metallization around the perimeter of the cavity. It has been clearly observed in the fabricated prototypes of the reference [Figure 31(f)] and proposed [Figure 31(g)] on-chip antennas. Four radiating circular patches embedded with metamaterial-inspired cross-shaped slots have been incorporated in the middle of the demetallized area of the top layer of the SIW cavity [Figure 31(g)]. Five layers of metal-silicon-metal-silicon-metal have been used to implement the on-chip antenna. A circle-shaped cavity has been engraved in the bottom silicon substrate, which has been placed just below the radiating patches [Figures 31(c) and 31(d)]. The lower silicon substrate has been positioned below the SIW cavity as observed in Figure 31(d). The ground plane metallization of the SIW cavity over the circular-shaped cavity has been removed [Figure 31(d)]. Excitation to the antenna has been provided by the coupling EM energy from the bottom of the lower silicon substrate to the radiating patches through the circular cavity. A cross-shaped feeding network (open-ended microstrip lines) has been designed on the bottom layer of the lower silicon substrate to enhance the impedance bandwidth of the antenna [Figures 31(b), 31(c)]. The inclusion of metamaterial and SIW has respectively enlarged the effective aperture area and minimized the surface wave excitations and substrate loss. The proposed antenna has exhibited an impedance bandwidth of 40 GHz ranging from 0.285 THz to 0.325 THz, as well as maximum gain of 8.05 dBi at 0.305 THz.

Furthermore, the application of metamaterial has been found in designing phased array antenna [92]. This phased array antenna consists of a metamaterial-inspired SIW CBSA, a novel series fed network, and CRLH 4-bit digital phase shifters. The phase shifters have been placed in the series fed network. Different phase shifts have been applied between the antenna elements by changing the on-off states of the p-i-n diodes mounted on the interdigital capacitor fingers of the digital phase shifters. Hence, the beam steering has been obtained at a specific frequency. Another CRLH SIW leaky-wave structure has been reported in [93]. The radiation characteristics of the antenna has been investigated with the curved version of the antenna. It has been observed that the curved CRLH SIW leaky-wave antenna has exhibited beam steering of about  $80^\circ$  through the frequency scanning.

A very unique approach of designing a metamaterial-based SIW leaky-wave antenna has been presented in [94]. The complexity involved in drilling holes and inserting metallization in the holes in formation of SIW has been significantly minimized by replacing the metallic vias with metamaterial such as CSRR (Figure 3 in [94]). The formation of the side wall has been accomplished by etching two CSRRs on the top and bottom metallic layers of the substrate, and by placing their gaps in opposite directions (Figure 1(a) in [94]). The coupling between the two CSRRs is the reason that makes the structure behave like an electric dipole. This electric dipole can be excited by the vertically polarized electric field, which results in its behaving like a vertical wire. Thus, this unique structure of the sidewall can minimize the leakage loss along with providing a guided path to the EM wave. This unique structure of the CSRR-SIW has enhanced the propagation loss characteristics as compared to the conventional SIW. The formation of the CSRR-SIW based LWA has been accomplished by incorporating two unequal





**Figure 31.** Layout of Antenna on Chip (AOC): (a) top view of reference antenna, (b) back view of reference antenna, (c) relative positions of feedline, cavity, and radiating elements of reference antenna, (d) cross-sectional view of reference antenna, (e) top view of the proposed antenna, (f) fabricated structure of reference antenna, and (g) fabricated structure of proposed antenna. Adopted from [91].

slots on the top metallic layer of the waveguide (Figure 6 in [94]). The antenna has performed well in 5G frequency band ranging from 26.3 GHz to 28 GHz as well as exhibited a directional radiation pattern of maximum gain 8 dBi. A detailed analysis of the CSRR-SIW has been presented in [95]. The designs of CSRR-SIW-based periodic LWAs for X-band and Ka-band applications have also been reported in [95].

A novel wideband SIW based split-ring resonator antenna has been reported in [96]. The detailed design descriptions of the coaxial to CPW and CPW to SIW transition have been demonstrated. Smooth propagation modes conversion from coaxial to CPW and CPW to SIW is necessary to obtain wideband performance. The E field distribution (Figure 6 in [96]) in the designed back-to-back transition prototype has shown that the coaxial mode has been generated at the input terminal (at the connector), CPW mode generated at the end of the coaxial to CPW transition, and finally, the SIW mode generated at the end of the CPW to SIW transition. Hence, the designed transition has exhibited a wider impedance



bandwidth (26 GHz to 40 GHz). Further, a wideband SIW two-stage power divider has been designed (Figure 10 in [96]), to serve the purpose of the feeding network in designing the antenna array structure. This power divider consists of one input and four output ports. The power divider has exhibited low insertion loss over the bandwidth of 10 GHz (27 GHz to 37 GHz). The formation of the single antenna element has been achieved by etching two split-ring resonators on the top metallic layer of the circular SIW cavity (Figure 12 in [96]). The antenna has produced a fractional bandwidth (FBW) of 19.7% at the center frequency of 30.5 GHz (frequency range: 27.5 GHz to 33.5 GHz) as well as obtained a maximum gain of 7.7 dBi. Finally, the formation of the  $2 \times 2$  antenna array structure has been accomplished by connecting four single antenna elements to the four output ports of the wideband two-stage power divider (Figure 19 in [96]). The antenna array has exhibited a wide FBW of 23% at the center frequency of 30.5 GHz (frequency range: 27 GHz to 34 GHz). Maximum directivity of 15 dBi has been obtained at 30 GHz by the proposed antenna array. Another novel design of wideband high-gain air-via metamaterial loaded Luneburg lens antenna for Ka-band application has been presented in [97]. The Luneburg lens has been illuminated by a SIW horn antenna. Thus, the SIW horn antenna has been used as a source of the Luneburg lens. The Luneburg lens has been integrated with the SIW horn antenna through the three-step air-via metamaterial (three different diameters of air-via have been used) transition. This transition has been loaded in front of the SIW horn antenna to obtain wide impedance bandwidth. The formation of the Luneburg lens (Figure 10 in [97]) has been accomplished by using five concentric regions of five different diameters of air-via metamaterial unit cells for smooth variation of the refractive index and to obtain better wave focusing effect. This design technique has brought miniaturization to the Luneburg lens. Finally, it has been observed that the SIW horn-fed Luneburg lens antenna has exhibited wide impedance bandwidth, ranging from 16 GHz to 28 GHz, along with a gain variation of 12.5 dBi to 17 dBi in the band of 18 GHz to 27 GHz.

The application of metamaterial has also been found in the design of bow-tie antenna [98]. A CSRR-SIW feeding has been used to feed the bow-tie antenna for obtaining the broadband performance. Unlike the reported designs of the conventional single periodic (SP) CRLH SIW leaky-wave antennas [70–72], a novel double periodic (DP) CRLH SIW leaky-wave antenna has been proposed in [99]. The loading of DP-CRLH unit cell has resulted in a new RH leaky-wave behavior below the LH passband. Thus, a new RH leaky-wave radiation pattern (forward radiation) has been obtained below the LH band. Moreover, the beam steering has also been achieved through the frequency scanning from conventional LH to RH region.

## 5. LIMITATIONS

Getting through the extensive literature review, it has been understood that the inclusion of metamaterial-inspired slots in the SIW cavities has led to operating the SIW CBSAs below the waveguide cut-off frequency (LH region), and hence, the miniaturization in antenna design has been obtained. Furthermore, the periodical repetition of the interdigital slots on the SIW transmission line has brought miniaturization in the design of SIW leaky-wave antennas (LWAs) by resonating the SIW LWAs at LH frequency region (below waveguide cut-off frequency). Moreover, application of the metamaterial has been found in beam steering, polarization flexibility, gain, and bandwidth enhancement and inter antenna elements' isolation improvement. Recently, the application of metamaterial has also been found in designing the suitable alternative to the SIW. Apart from discussing many advantages of metamaterial-based SIW antennas, some limitations have also been identified by the authors, which has been mentioned in this section. Some suitable solutions to these design restrictions have been proposed by the authors, which need further rigorous investigations. In the low frequency application, the size of the SIW (especially width of SIW) becomes large, and hence, it is easier to implement transverse slots on the top metallic layer of SIW. The width of the SIW is significantly reduced in high-frequency applications. Further reduction in the size of SIW can be possible by suitable alternatives, such as substrate integrated folded waveguide (SIFW) or half-mode substrate integrated waveguide (HMSIW) technology. SIFW/HMSIW reduces the size of SIW by a factor of the half. Thus, in mm-wave applications (30 GHz–300 GHz), the design of metamaterial-based SIW/SIFW/HMSIW CBSAs or LWAs will be very difficult, as the integration of transverse interdigital slots in the limited space of the top metallic layer of the SIW-TL/SIFW-TL/HMSIW-TL will be more complex. Hence, in mm-

**Table 4.** Summary of performances and design limitations of metamaterial-based SIW antennas.

Application of Metamaterial in Miniaturization of SIW Cavity-Backed Slot Antennas (CBSA)						
Reference	Design Technique	Operating Frequency (GHz)	Antenna Dimensions	Miniaturization Factor (%)	Antenna Gain (dBi)	Limitation
[63]	CRLH-TL Metamaterial & SIW CBSA	2.15	$0.18\lambda_0 \times 0.15\lambda_0 \times 0.02\lambda_0$	87	3.6	Limited space on the top metallic layer of SIW cavity to accommodate more interdigital capacitor fingers to enhance the capacitive effect.
[64]	CRLH-TL Metamaterial & SIW CBSA	2.45	$0.61\lambda_0 \times 0.39\lambda_0 \times 0.02\lambda_0$	79.74	5.35	————
[65]	CRLH-TL Metamaterial & SIW	SIW TL cut-off frequency: 11.3 GHz. One-stage open-ended antenna: $-1^{\text{st}}$ order resonance (LH region): 7.26 GHz. two-stage open-ended antenna: $-2^{\text{nd}}$ & $-1^{\text{st}}$ order resonances (LH region): 6.858 GHz & 7.31 GHz. One-stage short-ended antenna: $-1^{\text{st}}$ order resonance (LH region): 7.75 GHz.	One-stage open-ended antenna: $0.265\lambda_0 \times 0.318\lambda_0$ two-stage open-ended antenna: $0.48\lambda_0 \times 0.33\lambda_0$ One-stage short-ended antenna: $0.296\lambda_0 \times 0.335\lambda_0$ two-stage short-ended antenna: $0.506\lambda_0 \times 0.343\lambda_0$	Not available [antenna resonates below the waveguide cut-off frequency ( $-2^{\text{nd}}$ & $-1^{\text{st}}$ order resonances), thus, miniaturization has been obtained]	1-stage open-ended: 3.16 2-stage open-ended: 4.95 1-stage short-ended: 4.31 2-stage short-ended: 6.83	————

Application of Metamaterial in Gain Enhancement of SIW Slot Antenna (SA)/Leaky-Wave Antenna (LWA)						
Reference	Design Technique	Operating Frequency (GHz)	Gain of Reference Antenna (dBi)	Gain of Antenna with Metamaterial (dBi)	Gain Improvement (dBi)	Limitation
[66]	Cross Circular Loop Resonator (CCLR) Metamaterial, low impedance metamaterial (EVL-MNZ) slab & SIW SA	9.8	SIW SA: 3	8.8	5.8	Enlarged overall dimensions.
[67]	Low impedance metamaterial (EVL-MNZ) slab & SIW SA	9.8	SIW SA: 3	8.24	5.24	Enlarged overall dimensions.
[68]	Low impedance metamaterial (EVL-MNZ) slab & SIW SA	9.78	SIW SA: 3	11.3	8.3	Enlarged overall dimensions.
[69]	CRLH-TL Metamaterial & SIW LWA	3–4.8	CRLH-TL LWA without SIW: 3.65 dBi	CRLH-TL LWA with SIW: 5.8 dBi	2.15	————

Application of Metamaterial in Beam Steering of SIW Leaky-Wave Antenna (LWA)					
Reference	Design Technique	Operating Frequency Band (GHz)	Beam Steering (Back-fire to End-fire)	Antenna Gain (dBi)	Limitation
[70]	CRLH-TL Metamaterial, SIW & Half-mode SIW (HMSIW) LWA	Balanced SIW CRLH-TL LWA: 8.5–10 (LH region) & 10–> 12 (RH region) transition frequency: 10 GHz. Unbalanced HMSIW CRLH-TL LWA: 8.7–9.6 (LH region) & 10.6–> 12 (RH region)	Balanced SIW CRLH-TL LWA: LH region (back-fire radiation): $-70^\circ < 0^\circ$ RH region (end-fire radiation): $> 0^\circ + 60^\circ$ broad-side radiation at $0^\circ$ (10 GHz). Unbalanced HMSIW CRLH-TL LWA: LH region: $-75^\circ > 0^\circ$ RH region: $> 0^\circ + 35^\circ$	Balanced SIW CRLH-TL LWA: 10.82 dBi Unbalanced HMSIW CRLH-TL LWA: approximately 10 dBi.	Enlarged length LWAs. Lengths of LWAs are large as compared to the wavelength. (Approximately $3.37\lambda_0$ & $3.86\lambda_0$ )
[71]	CRLH-TL Metamaterial & SIW LWA	1 <sup>st</sup> Balanced CRLH band: 7.1–8.7 (LH region) & 8.7–10.75 (RH region) transition frequency: 8.7 GHz. 2 <sup>nd</sup> unbalanced CRLH band: 15–19 (LH region) & 19.25–21.75 (RH region) New RH band: 12.6–13.4.	1 <sup>st</sup> Balanced CRLH band: LH region: $-78^\circ < 0^\circ$ RH region: $> 0^\circ + 78^\circ$ broad-side radiation at $0^\circ$ (8.7 GHz). 2 <sup>nd</sup> unbalanced CRLH band: LH region: $-40^\circ < 0^\circ$ RH region: $> 0^\circ + 20^\circ$ New RH band: $+22^\circ + 54^\circ$ .	1 <sup>st</sup> Balanced CRLH band: 15.3 dBi. 2 <sup>nd</sup> unbalanced CRLH band: 17.3 dBi. New RH band: 16.1 dBi.	Enlarged length LWA. Length of LWA is large as compared to the wavelength. (Approximately $6.53\lambda_0$ )
[72]	Multi-layered CRLH-TL Metamaterial & SIW LWA	Balanced CRLH band: 8–9 (LH band), & 9–13 (RH band) transition frequency: 8.9 GHz.	LH region: $-66^\circ < 0^\circ$ . RH region: $> 0^\circ + 78^\circ$ . Broadside radiation obtained at $0^\circ$ (8.9 GHz).	10	Enlarged length LWA. Length of LWA is large as compared to the wavelength. ( $4.5\lambda_0$ )
[73]	CRLH-TL Metamaterial & HMSIW LWA	Balanced CRLH band: 13.5–< 16 (LH band), & > 16–17.8 (RH band) transition frequency: 16 GHz.	LH region: $-66^\circ < 0^\circ$ . RH region: $> 0^\circ + 20^\circ$ . Broadside radiation at $0^\circ$ (16 GHz).	16	Enlarged length LWA. Length of LWA is large as compared to the wavelength. ( $4.85\lambda_0$ )
[74]	CRLH-TL Metamaterial & SIW LWA	Balanced CRLH band: 55–< 60 (LH band), & > 60–65 (RH band) transition frequency: 60 GHz.	LH region: $-30^\circ < 0^\circ$ . RH region: $> 0^\circ + 30^\circ$ . Broadside radiation at $0^\circ$ (60 GHz).	10.1	Length of LWA is large as compared to the wavelength. ( $7.33\lambda_0$ )
[75]	CRLH-TL Metamaterial & Eighth Mode SIW (EMSIW) LWA	Balanced CRLH band: 9–< 11.5 (LH band), & > 11.5–13.5 (RH band) transition frequency: 11.5 GHz.	LH region: $-64^\circ < 0^\circ$ . RH region: $> 0^\circ + 43^\circ$ . Broadside radiation at $0^\circ$ (11.5 GHz).	17.96	Length of LWA is large as compared to the wavelength. ( $5\lambda_0$ )
[76]	Mushroom type Metamaterial & SIW Aperture Antenna	13.3–16.7; LH region: 13.3–15.1, Band-gap region: > 15.1 & transition frequency between the LH and band-gap region: 15 GHz.	$-90^\circ - 0^\circ$	Not available	—

Application of Metamaterial/Metasurface in Minimizing Mutual Coupling in SIW-Based MIMO Antenna							
Reference	Design Technique	Operating Frequency (GHz)	Isolation without Metamaterial (dB)	Isolation with Metamaterial (dB)	Isolation Improvement (dB)	Antenna Gain (dBi)	Limitation
[78]	Metamaterial: Double Layer Mushroom Wall, & SIW CBSA	2.396–2.45	Parallel positioned antennas: $S_{31} = S_{42} \cong -20$ Orthogonally positioned antennas: $S_{21} = S_{32} = S_{43} = S_{41} < -40$	Parallel positioned antennas: $S_{31} = S_{42} \cong -42$ Orthogonally positioned antennas: $S_{21} = S_{32} = S_{43} = S_{41} \cong -42$	$S_{31}$ & $S_{42} = 16$ dB over the entire operating frequency band and 22 dB in the frequency band of 2.415 GHz–2.445 GHz. $S_{21}$ , $S_{32}$ , $S_{43}$ & $S_{41}$ are unaffected.	4	Bulky structure due to insertion of double layer mushroom metamaterial wall.
[74]	Metamaterial shield & SIW CRLH-TL LWA	55–65	$S_{13} \cong -25$	$S_{13} \cong -30$	42.5 (maximum improvement)	10.16	Enlarged length LWA.
[79]	Metamaterial, Metal Fence Isolator & SIW SA	X-band & Ku-band: 8.7–8.95 10.75–10.9 11–11.15 12–12.3 13.5–13.75 14.8–14.95	$S_{12} \cong -10$	$S_{12} < -15$	13 (average improvement over the entire operating frequency band) & maximum 20 dB	12.5	Bulky structure due to 3D antenna configuration and insertion of metal fence isolator between the radiating slots.
[80]	Metamaterial, Metal Fence Isolator & SIW Longitudinal Slot Array Antenna (SIWLSAA)	0.2–1	$S_{12} \cong -63$	$S_{12} \cong -98$	35 (maximum improvement)	1.75	3D antenna configuration has made the overall design bulky.
[81]	Metasurface & SIW	125–300	$S_{12} < -20$	$S_{12} < -30$	Isolation improvement due to SIW: 50 dB (Maximum improvement) & 25 dB (Average improvement)	7.51–40.08 (over the entire operating frequency band) [Metasurface is responsible for high gain]	—

Application of Metamaterial in Broadening of Impedance Bandwidth of SIW-Based Antennas						
Reference	Design Technique	Impedance Bandwidth of Reference Antenna (GHz)	Impedance Bandwidth of Antenna with Metamaterial (GHz)	Bandwidth Improvement (%)	Antenna Gain (dBi)	Limitation
[82]	Mushroom type metamaterial & SIW horn antenna	Very narrow BW. Resonates at 14.7 GHz.	14.4–16	FBW: 10.6 BW improvement: Not available	6.3–8.1 (over the operating frequency band)	Loading of mushroom-type metamaterial slab in front of horn aperture has enlarged the overall antenna length.
[83]	Metamaterial, SRR & SIW	27.6–28.7 (1.1 GHz)	Approximately 26–29.7 (3.7 GHz)	FBW: 13.2 Improvement: 42.3	6.8	—
[84]	CRLH-TL metamaterial, Unequal U-shaped slots & SIW aperture antenna	SIW aperture antenna with CRLH-TL metamaterial: resonates at 15.93 GHz. FBW: 2.13%	CRLH-TL SIW aperture antenna with unequal size U-shaped slots: 11.88–14.05 GHz. FBW: 16.74%	Improvement in FBW: 14.31%	6.1 dBi at 12.1 GHz.	—

Application of Metamaterial/Metasurface for Performance Improvement of SIW Based On-chip Antenna in THz Frequency Band						
Reference	Design Technique & Process	Operating Frequency Band (THz)	Antenna Dimensions	Antenna Fractional Bandwidth (FBW)	Antenna Gain (dBi)	Limitation
[88]	Metasurface & SIW	0.45–0.5 (50 GHz)	$1.21\lambda_0 \times 1.21\lambda_0 \times 0.196\lambda_0$ at 0.45 GHz.	10.5%	7.4 dBi	—
[89]	Metasurface & SIW	0.2–0.22 (20 GHz)	$1 \times 1 \times 0.265 \text{ mm}^3$	Not available	9 dBi at 0.21 THz.	—
[90]	Metamaterial & SIW	0.3–0.31 (10 GHz)	$2 \times 1.5 \times 0.0001 \text{ mm}^3$	Not available	1.75 dBi at 305 GHz.	—
[91]	Metamaterial & SIW	0.285–0.325 (40 GHz)	$1.35 \times 1 \times 0.06 \text{ mm}^3$	13.11%	8.05 dBi at 305 GHz.	—

wave applications, instead of using transverse interdigital slot, multilayer CRLH metamaterial unit cell can be a suitable choice for minimizing difficulties in obtaining beam steering and polarization flexibility. Difficulty in accommodating transverse interdigital slot is due to the inclusion of more than one finger (typically 5 or 6 fingers), whereas a single transverse slot of multilayer CRLH metamaterial unit cell can be easily fitted. Tilting a transverse interdigital slot for achieving polarization flexibility might be a difficult task as compared to tilting a single transverse slot of the multilayer CRLH-TL metamaterial. Further, in mm-wave application instead of using four complementary spiral resonators, only two spiral/split-ring resonators can be easily accommodated on the HMSIW-TL/SIFW-TL, which

can serve the purpose of obtaining beam steering. Typically, the incorporation of the metamaterial wall between the SIW CBSAs to improve the isolation has made the antenna profile large. To bring miniaturization in the antenna design, 2D metamaterial shield can be a suitable choice for improving the isolation between the SIW LWAs/CBSAs, rather to use the 3D metamaterial wall. The enhancement of impedance bandwidth of a thin ( $h = 0.05\lambda_0$ ) SIW  $H$ -plane horn antenna has been obtained by integrating an array ( $4 \times 7$ ) of metamaterial unit cells in front of horn aperture [42]. Although the attainment of wider impedance bandwidth has been possible (beyond 10%), it cannot be denied that the length of the antenna has been increased. Thus, the loading of a metamaterial slab in front of a SIW  $H$ -plane horn antenna and on the top of the SIW slot antenna (SA) for enhancing the bandwidth and antenna gain respectively has resulted in enlarging the overall antenna dimensions, hence difficult to accommodate the antenna in compact devices. Furthermore, Table 4 is presented in this section which consists of the summary of metamaterial-based SIW CBSAs, LWAs, aperture antennas, and horn antennas performances as well as design limitations. The authors believe that Table 4 yields a clear view of SIW-based antennas' attractive features under the influence of the metamaterial, as well as its design limitations to the readers.

## 6. CONCLUSION

A comprehensive study on the physics behind the unique properties of the metamaterials, as well as on the applications of the CRLH-TL metamaterials in the microstrip patch and SIW-based antenna designs, have been presented in this article. The typical configuration of SIW and its  $S$ -parameter and dispersion characteristics have been presented. The designs of SNG and DNG materials have been reported. The methodology of obtaining the dispersion characteristics of the CRLH-TL metamaterial unit cell by analyzing its equivalent circuit as well as the technique of realization of the CRLH-TL metamaterial unit cell by the distributed element has also been discussed. A rigorous survey on the performance improvement of the microstrip patch antennas under the influence of metamaterial has been carried out. Moreover, several applications of CRLH-TL metamaterial in designing of SIW CBSAs, SIW LWAs, SIW aperture antennas, and SIW horn antennas have been extensively reviewed. The working principles of the metamaterial loaded SIW CBSAs, SIW LWAs, SIW aperture antennas, SIW  $H$ -plane horn antennas, and SIW on-chip antennas have been elaborated. Besides these, a novel design of CSRR-SIW which is a suitable alternative to the conventional SIW technology has been described in this article. Despite several advantages in the application of metamaterials in SIW-based antenna designing, some limitations have also been identified by the authors. Some approximate ideas in resolving these limitations have been introduced by the authors. Finally, it can be stated that this review on the metamaterial-based microstrip patch and SIW antennas can be considered as the motivation and potential reference to the researchers in performing further advanced research on the metamaterial applications in microstrip and SIW-based antenna technology.

**Note:** All the figures (except Figures 28, 29, 30, and 31) and tables (except Table 3) presented in this article have been recreated by the authors.

## REFERENCES

1. Jung, J., W. Choi, and J. Choi, "A small wideband microstrip-fed monopole antenna," *IEEE Microwave and Wireless Component Letters*, Vol. 15, 703–705, 2005.
2. Tseng, C.-F., C.-L. Huang, and C.-H. Hsu, "Microstrip fed monopole antenna with a shorted parasitic element for wideband application," *Progress in Electromagnetics Research Letters*, Vol. 7, 115–125, 2009.
3. Luk, K. M. and S. H. Wong, "A printed high-gain monopole antenna for indoor wireless LANs," *Microwave and Optical Technology Letters*, Vol. 41, 177–180, 2004.
4. Sihvola, A., "Metamaterials in electromagnetics," *Metamaterials*, Vol. 2, 2–11, 2007.
5. Cui, T. J., D. R. Smith, and R. Liu, *Metamaterials: Theory, Design and Applications*, Springer, 2009.



6. Ziolkowski, R. W. and A. Erentok, "Metamaterial-based efficient electrically small antennas," *IEEE Transactions on Antennas and Propagation*, Vol. 54, 2113–2130, 2006.
7. Alù, A., F. Bilotti, N. Engheta, and L. Vegni, "Subwavelength, compact, resonant patch antennas loaded with metamaterials," *IEEE Transactions on Antennas and Propagation*, Vol. 55, 13–25, 2007.
8. Ouedraogo, R. O., E. J. Rothwell, A. R. Diaz, K. Fuchi, and A. Temme, "Miniaturization of patch antennas using a metamaterial-inspired technique," *IEEE Transactions on Antennas and Propagation*, Vol. 60, 2175–2182, 2012.
9. Panda, P. K. and D. Ghosh, "Isolation and gain enhancement of patch antennas using EMNZ superstrate," *International Journal of Electronics and Communication (AEU)*, Vol. 86, 164–170, 2018.
10. Li, D., Z. Szabo, X. Qing, E.-P. Li, and Z. N. Chen, "A high gain antenna with an optimized metamaterial inspired superstrate," *IEEE Transactions on Antennas and Propagation*, Vol. 60, 6018–6023, 2012.
11. Guo, Y., G. Goussetis, A. P. Feresidis, and J. C. Vardaxoglou, "Efficient modeling of novel uniplanar left-handed metamaterials," *IEEE Transactions on Microwave Theory and Techniques*, Vol. 53, 1462–1468, 2005.
12. Alsath, M. G. N., M. Kanagasabai, and B. Balasubramanian, "Implementation of slotted meander-line resonators for isolation enhancement in microstrip patch antenna arrays," *IEEE Antennas and Wireless Propagation Letters*, Vol. 12, 15–18, 2013.
13. Thummaluru, S. R. and R. K. Chaudhary, "Mu-negative metamaterial filter-based isolation technique for MIMO antennas," *Electronics Letters*, Vol. 53, 644–646, 2017.
14. Pozar, D. M., *Microwave Engineering*, John Wiley & Sons, 2011.
15. Xu, F. and K. Wu, "Guided-wave and leakage characteristics of substrate integrated waveguide," *IEEE Transactions on Microwave Theory and Techniques*, Vol. 53, 66–73, 2005.
16. Kordiboroujeni, Z. and J. Bornemann, "Designing the width of substrate integrated waveguide structures," *IEEE Microwave and Wireless Components Letters*, Vol. 23, 518–520, 2013.
17. Alu, A., N. Engheta, A. Erentok, and R. W. Ziolkowski, "Single-negative, double-negative, and low-index metamaterials and their electromagnetic applications," *IEEE Antennas and Propagation Magazine*, Vol. 49, 23–36, 2007.
18. Miliadis, C., R. B. Andersen, P. I. Lazaridis, Z. D. Zaharis, B. Muhammad, J. T. B. Kristensen, A. Mihovska, and D. D. S. Hermansen, "Metamaterial-inspired antennas: A review of the state of the art and future design challenges," *IEEE Access*, Vol. 09, 89846–89865, 2021.
19. Jokanovic, B., R. H. Geschke, T. S. Beukman, and V. Milosevic, "Metamaterials: Characteristics, design and microwave applications," *SAIEE African Research Journal*, Vol. 101, 82–92, 2010.
20. Veselago, V. G., "The electrodynamics of substances with simultaneously negative values of  $\epsilon$  and  $\mu$ ," *Soviet Physics Uspekhi*, Vol. 10, 509–514, 1968.
21. Pendry, J. B., A. J. Holden, W. J. Stewart, and I. Youngs, "Extremely low frequency plasmons in metallic mesostructures," *Physical Review Letters*, Vol. 76, 4773–4776, 1996.
22. Pendry, J. B., A. J. Holden, D. J. Robbins, and W. J. Stewart, "Magnetism from conductors and enhanced nonlinear phenomena," *IEEE Transactions on Microwave Theory and Techniques*, Vol. 47, 2075–2081, 1999.
23. Dong, Y., H. Toyao, and T. Itoh, "Design and characterization of miniaturized patch antennas loaded with complementary split-ring resonators," *IEEE Transactions on Antennas and Propagation*, Vol. 60, 772–785, 2012.
24. Falcone, F., T. Lopetegui, M. A. G. Laso, J. D. Baena, J. Bonache, M. Beruete, R. Marqués, F. Martín, and M. Sorolla, "Babinet principle applied to the design of metasurfaces and metamaterials," *Physical Review Letters*, Vol. 93, 197401-1–4, 2004.
25. Smith, D. R., W. J. Padilla, D. C. Vier, S. C. Nemat-Nasser, and S. Schultz, "Composite medium with simultaneously negative permeability and permittivity," *Physical Review Letters*, Vol. 84, 4184–4187, 2000.

26. Lai, A., C. Caloz, and T. Itoh, "Composite right/left-handed transmission line metamaterials," *IEEE Microwave Magazine*, Vol. 05, 34–50, 2004.
27. Alibakhshikenari, M., B. S. Virdee, L. Azpilicueta, M. Naser-Moghadasi, M. O. Akinsolu, C. H. See, B. Liu, R. A. ABD-Alhameed, F. Falcone, I. Huynen, T. A. Denidni, and E. Limiti, "A comprehensive survey of metamaterial transmission-line based antennas: Design, challenges, and applications," *IEEE Access*, Vol. 08, 144778–144808, 2020.
28. Alibakhshikenari, M., "Printed planar patch antennas based on metamaterial," *International Journal of Electronics Letters*, Vol. 02, 37–42, 2014.
29. Sadeghzadeh, R. A., M. Alibakhshikenari, and M. Naser-Moghadasi, "UWB antenna based on SCRLH-TLs for portable wireless devices," *Microwave and Optical Technology Letters*, Vol. 58, 69–71, 2016.
30. Alibakhshikenari, M., A. Andujar, and J. Anguera, "New compact printed leaky-wave antenna with beam steering," *Microwave and Optical Technology Letters*, Vol. 58, 215–217, 2016.
31. Alibakhshikenari, M., M. Naser-Moghadasi, R. A. Sadeghzadeh, and B. S. Virdee, "Metamaterial-based antennas for integration in UWB transceivers and portable microwave handsets," *International Journal of RF and Microwave Computer-Aided Engineering*, Vol. 26, 88–96, 2016.
32. Alibakhshikenari, M., M. Naser-Moghadasi, R. A. Sadeghzadeh, B. S. Virdee, and E. Limiti, "New compact antenna based on simplified CRLH-TL for UWB wireless communication systems," *International Journal of RF and Microwave Computer-Aided Engineering*, Vol. 26, 217–225, 2016.
33. Alibakhshikenari, M., M. Naser-Moghadasi, B. S. Virdee, A. Andujar, and J. Anguera, "Compact antenna based on a composite right/left-handed transmission line," *Microwave and Optical Technology Letters*, Vol. 57, 1785–1788, 2015.
34. Alibakhshikenari, M., M. Naser-Moghadasi, and R. A. Sadeghzadeh, "The resonating MTM-based miniaturized antennas for wide-band RF-microwave systems," *Microwave and Optical Technology Letters*, Vol. 57, 2339–2344, 2015.
35. Alibakhshikenari, M., B. S. Virdee, A. Ali, and E. Limiti, "A novel monofilar-archimedean metamaterial inspired leaky-wave antenna for scanning application for passive radar system," *Microwave and Optical Technology Letters*, Vol. 60, 2055–2060, 2018.
36. Alibakhshikenari, M. and M. Naser-Moghadasi, "Novel UWB miniaturized integrated antenna based on CRLH metamaterial transmission lines," *International Journal of Electronics and Communication (AEU)*, Vol. 69, 1143–1149, 2015.
37. Alibakhshikenari, M., M. Naser-Moghadasi, R. A. Sadeghzadeh, B. S. Virdee, and E. Limiti, "Bandwidth extension of planar antennas using embedded slits for reliable multiband RF communications," *International Journal of Electronics and Communication (AEU)*, Vol. 70, 910–919, 2016.
38. Alibakhshikenari, M., M. Naser-Moghadasi, R. A. Sadeghzadeh, B. S. Virdee, and E. Limiti, "Travelling-wave antenna based on metamaterial transmission line structure for use in multiple wireless communication applications," *International Journal of Electronics and Communication (AEU)*, Vol. 70, 1645–1650, 2016.
39. Alibakhshikenari, M., B. S. Virdee, and E. Limiti, "Wideband planar array antenna based on SCRLH-TL for airborne synthetic aperture radar application," *Journal of Electromagnetic Waves and Applications*, Vol. 32, No. 12, 1586–1599, 2018.
40. Alibakhshikenari, M., M. Naser-Moghadasi, and R. A. Sadeghzadeh, "Bandwidth and radiation specifications enhancement of monopole antennas loaded with split ring resonators," *IET Microwaves, Antennas & Propagation*, Vol. 09, 1487–1496, 2015.
41. Alibakhshikenari, M., M. Naser-Moghadasi, and R. A. Sadeghzadeh, "Composite right-left-handed-based antenna with wide applications in very-high frequency-ultra-high frequency bands for radio transceivers," *IET Microwaves, Antennas & Propagation*, Vol. 09, 1713–1726, 2015.
42. Alibakhshikenari, M., M. Naser-Moghadasi, R. A. Sadeghzadeh, B. S. Virdee, and E. Limiti, "Periodic array of complementary artificial magnetic conductor metamaterials-based multiband antennas for broadband wireless Transceivers," *IET Microwaves, Antennas & Propagation*, Vol. 10, 1682–1691, 2016.

43. Alibakhshikenari, M., B. S. Virdee, A. Ali, and E. Limiti, "Miniaturised planar-patch antenna based on metamaterial L-shaped unit-cells for broadband portable microwave devices and multiband wireless communication systems," *IET Microwaves, Antennas & Propagation*, Vol. 12, 1080–1086, 2018.
44. Alibakhshikenari, M., B. S. Virdee, C. H. See, R. Abd-Alhameed, A. Ali, F. Falcone, and E. Limiti, "Wideband printed monopole antenna for application in wireless communication systems," *IET Microwaves, Antennas & Propagation*, Vol. 12, 1222–1230, 2018.
45. Alibakhshikenari, M., B. S. Virdee, M. Khalily, P. Shukla, C. H. See, R. Abd-Alhameed, F. Falcone, and E. Limiti, "Beam-scanning leaky-wave antenna based on CRLH-metamaterial for millimetre-wave applications," *IET Microwaves, Antennas & Propagation*, Vol. 13, 1129–1133, 2019.
46. Alibakhshikenari, M., M. Khalily, B. S. Virdee, A. Ali, P. Shukla, C. H. See, R. Abd-Alhameed, F. Falcone, and E. Limiti, "Double-port slotted-antenna with multiple miniaturized radiators for wideband wireless communication systems and portable devices," *Progress in Electromagnetics Research C*, Vol. 90, 1–13, 2019.
47. Alibakhshikenari, M., B. S. Virdee, C. H. See, R. Abd-Alhameed, F. Falcone, and E. Limiti, "Overcome the limitations of performance parameters of on-chip antennas based on metasurface and coupled Feeding approaches for applications in system-on-chip for THz integrated-circuits," *IEEE Asia-Pacific Microwave Conference*, 2019.
48. Alibakhshikenari, M., B. S. Virdee, M. Khalily, C. H. See, R. Abd-Alhameed, F. Falcone, T. A. Denidni, and E. Limiti, "High-gain on-chip antenna design on silicon layer with aperture excitation for terahertz applications," *IEEE Antennas and Wireless Propagation Letters*, Vol. 19, 1576–1580, 2020.
49. Alibakhshikenari, M., B. S. Virdee, C. H. See, R. Abd-Alhameed, F. Falcone, and E. Limiti, "Impedance matching network based on metasurfaces (2-d metamaterials) for electrically small antennas," *IEEE International Symposium on Antennas and Propagation and North America Radio Science Meeting*, 2020.
50. Alibakhshikenari, M., B. S. Virdee, P. Shukla, Y. Wang, L. Azpilicueta, M. Naser-Moghadasi, C. H. See, I. Elfergani, C. Zebiri, R. Abd-Alhameed, I. Huynen, J. Rodriguez, T. A. Denidni, F. Falcone, and E. Limiti, "Impedance bandwidth improvement of a planar antenna based on metamaterial-inspired T-matching network," *IEEE Access*, Vol. 09, 67916–67927, 2021.
51. Alibakhshikenari, M., B. S. Virdee, P. Shukla, N. O. Parchin, L. Azpilicueta, C. H. See, R. Abd-Alhameed, F. Falcone, I. Huynen, T. A. Denidni, and E. Limiti, "Metamaterial-inspired antenna array for application in microwave breast imaging systems for tumor detection," *IEEE Access*, Vol. 08, 174667–174678, 2020.
52. Alibakhshikenari, M., F. Babaeian, B. S. Virdee, S. Aissa, L. Azpilicueta, C. H. See, A. A. Althwayb, I. Huynen, R. Abd-Alhameed, F. Falcone, and E. Limiti, "A comprehensive survey on various decoupling mechanisms with focus on metamaterial and metasurface principles applicable to SAR and MIMO antenna systems," *IEEE Access*, Vol. 08, 192965–193004, 2020.
53. Alibakhshikenari, M., B. S. Virdee, P. Shukla, C. H. See, R. Abd-Alhameed, F. Falcone, and E. Limiti, "Meta-surface wall suppression of mutual coupling between microstrip patch antenna arrays for THz-band applications," *Progress in Electromagnetics Research Letters*, Vol. 75, 105–111, 2018.
54. Alibakhshikenari, M., B. S. Virdee, P. Shukla, C. H. See, R. Abd-Alhameed, M. Khalily, F. Falcone, and E. Limiti, "Antenna mutual coupling suppression over wideband using embedded periphery slot for antenna arrays," *Electronics*, Vol. 07, 198, 2018.
55. Alibakhshikenari, M., B. S. Virdee, C. H. See, R. Abd-Alhameed, A. H. Ali, F. Falcone, and E. Limiti, "Study on isolation improvement between closely-packed patch antenna arrays based on fractal metamaterial electromagnetic bandgap structures," *IET Microwaves, Antennas & Propagation*, Vol. 12, 2241–2247, 2018.

56. Alibakhshikenari, M., B. S. Virdee, P. Shukla, C. H. See, R. Abd-Alhameed, F. Falcone, K. Quazzane, and E. Limiti, "Isolation enhancement of densely packed array antennas with periodic MTM-photonibandgap for SAR and MIMO systems," *IET Microwaves, Antennas & Propagation*, Vol. 14, 183–188, 2020.
57. Alibakhshikenari, M., M. Khalily, B. S. Virdee, C. H. See, R. Abd-Alhameed, and E. Limiti, "Mutual coupling suppression between two closely placed microstrip patches using EM-bandgap metamaterial fractal loading," *IEEE Access*, Vol. 07, 23606–23614, 2019.
58. Alibakhshikenari, M., M. Khalily, B. S. Virdee, C. H. See, R. Abd-Alhameed, and E. Limiti, "Mutual-coupling isolation using embedded metamaterial EM bandgap decoupling slab for densely packed array antennas," *IEEE Access*, Vol. 07, 51827–51840, 2019.
59. Alibakhshikenari, M., M. Vittori, S. Colangeli, B. S. Virdee, A. Andujar, J. Anguera, and E. Limiti, "EM isolation enhanced based on metamaterial concept in antenna array system to support full-duplex application," *IEEE Asia Pacific Microwave Conference*, 2017.
60. Alibakhshikenari, M., B. S. Virdee, M. Khalily, C. H. See, R. Abd-Alhameed, F. Falcone, and E. Limiti, "A new study to suppress mutual-coupling between waveguide slot array antennas based on metasurface bulkhead for MIMO systems," *IEEE Asia Pacific Microwave Conference*, 2018.
61. Alibakhshikenari, M., B. S. Virdee, and E. Limiti, "A technique to suppress mutual coupling in densely packed antenna arrays using metamaterial supersubstrate," *12th European Conference on Antennas and Propagation*, 2018.
62. Alibakhshikenari, M., B. S. Virdee, C. H. See, R. Abd-Alhameed, F. Falcone, A. Andujar, J. Anguera, and E. Limiti, "Study on antenna mutual coupling suppression using integrated metasurface isolator for SAR and MIMO applications," *48th European Microwave Conference*, 2018.
63. Saghati, A. P., A. P. Saghati, and K. Entesari, "An ultra-miniature SIW cavity-backed slot antenna," *IEEE Antennas and Wireless Propagation Letters*, Vol. 16, 313–316, 2016.
64. Lajevardi, M. E. and M. Kamyab, "Ultra-miniaturized metamaterial-inspired SIW textile antenna for off-body applications," *IEEE Antennas and Wireless Propagation Letters*, Vol. 16, 3155–3158, 2017.
65. Dong, Y. and T. Itoh, "Miniaturized substrate integrated waveguide slot antennas based on negative order resonance," *IEEE Transactions on Antennas and Propagation*, Vol. 58, 3856–3864, 2010.
66. Pandit, S., A. Mohan, and P. Ray, "A low-profile high-gain substrate integrated waveguide slot antenna with suppressed cross-polarization using metamaterial," *IEEE Antennas and Wireless Propagation Letters*, Vol. 16, 1614–1617, 2017.
67. Pandit, S., A. Mohan, and P. Roy, "Metamaterial-inspired low-profile high-gain slot antenna," *Microwave and Optical Technology Letters*, 1–6, 2019.
68. Pandit, S., A. Mohan, and P. Roy, "Square-ring metamaterial for radiation characteristics enhancement of an SIW cavity-backed slot antenna," *International Journal of RF and Microwave Computer-Aided Engineering*, e21981, 1–8, 2019.
69. Althuwayb, A. A., "Enhanced radiation gain and efficiency of a metamaterial-inspired wideband microstrip antenna using substrate integrated waveguide technology for sub-6 GHz wireless communications systems," *Microwave and Optical Technology Letters*, Vol. 63, 1892–1898, 2021.
70. Dong, Y. and T. Itoh, "Composite right/left-handed substrate integrated waveguide and half mode substrate integrated waveguide leaky-wave structures," *IEEE Transactions on Antennas and Propagation*, Vol. 59, 767–775, 2011.
71. Haghighi, S. S., A.-A. Heidari, and M. Movahhedi, "Three-band substrate integrated waveguide leaky-wave antenna based on composite right/left-handed structure," *IEEE Transactions on Antennas and Propagation*, Vol. 63, 4578–4582, 2015.
72. Nasimuddin, Z. N. Chen, and X. Qing, "Multilayered composite right/left-handed leaky-wave antenna with consistent gain," *IEEE Transactions on Antennas and Propagation*, Vol. 60, 5056–5062, 2012.

73. Sarkar, A., M. Adhikary, A. Sharma, A. Biswas, and M. J. Akhtar, "Composite right/left-handed compact and high-gain leaky-wave antenna using complementary spiral resonator on HMSIW for Ku band applications," *IET Microwaves, Antennas & Propagation*, Vol. 12, 1310–1315, 2018.
74. Alibakhshikenari, M., B. S. Virdee, C. H. See, R. A. Abd-Alhameed, F. Falcone, and E. Limiti, "High-isolation leaky-wave array antenna based on CRLH-metamaterial implemented on SIW with  $\pm 30^\circ$  frequency beam-scanning capability at millimetre-waves," *Electronics*, Vol. 8, 1–15, 2019.
75. Sarkar, A., A. Sharma, A. Biswas, and M. J. Akhtar, "EMSIW-based compact high gain wide full space scanning LWA with improved broadside radiation profile," *IEEE Transactions on Antennas and Propagation*, Vol. 67, 5652–5657, 2019.
76. Cai, Y., S. LI, T. Wu, and Y. Cao, "A simple configuration of beam steering substrate integrated waveguide aperture antenna loaded with metamaterials," *Microwave and Optical Technology Letters*, Vol. 64, 744–749, 2022.
77. Dong, Y. and T. Itoh, "Substrate integrated composite right-/left-handed leaky-wave structure for polarization-flexible antenna application," *IEEE Transactions on Antennas and Propagation*, Vol. 60, 760–771, 2012.
78. Zhai, G., Z. N. Chen, and X. Qing, "Enhanced isolation of a closely-spaced four-element MIMO antenna system using metamaterial mushroom," *IEEE Transactions on Antennas and Propagation*, Vol. 63, 3362–3370, 2015.
79. Alibakhshikenari, M., B. S. Virdee, C. H. See, R. Abd-Alhameed, F. Falcone, and E. Limiti, "Mutual-coupling reduction in metamaterial substrate integrated waveguide slotted antenna arrays using metal fence isolators for SAR and MIMO applications," *12th International Congress on Artificial Materials for Novel Wave Phenomena*, 2018.
80. Alibakhshikenari, M., B. S. Virdee, M. Khalily, C. H. See, R. Abd-Alhameed, F. Falcone, and E. Limiti, "New approach to suppress mutual coupling between longitudinal-slotted arrays based on SIW antenna loaded with metal-fences working on VHF/UHF frequency-bands: Study, investigation, and principle," *Asia-Pacific Microwave Conference*, 2018.
81. Alibakhshikenari, M. and B. S. Virdee, "Study on isolation and radiation behaviours of a  $34 \times 34$  array-antennas based on SIW and metasurface properties for applications in terahertz band over 125–300 GHz," *Optik*, Vol. 206, 163222, 2020.
82. Cai, Y., Y. Zhang, L. Yang, Y. Cao, and Z. Qian, "Design of low-profile metamaterials-loaded substrate integrated waveguide horn antenna and its array applications," *IEEE Transactions on Antennas and Propagation*, Vol. 65, 3732–3737, 2017.
83. Murad, N. A., M. W. Almesheshe, O. Ayop, and M. K. A. Rahim, "Wideband metamaterial substrate integrated waveguide antenna for millimeterwave applications," *IEEE International RF and Microwave Conference*, 2020.
84. Ameen, M., A. Mishra, and R. K. Chaudhary, "Compact open-ended SIW antenna based on CRLH-TL and U-shaped slots for Ku-band application," *International Journal of Electronics and Communication (AEU)*, Vol. 131, 1–11, 2021.
85. Kumari, V., W. Bhowmik, and S. Srivastava, "Design of high-gain SIW and HMSIW *H*-plane horn antenna using metamaterial," *International Journal of Microwave and Wireless Technologies*, Vol. 07, 713–720, 2015.
86. El-Nady, S., R. R. Elsharkawy, A. I. Affi, and A. S. Abd El-Hameed, "Performance improvement of substrate integrated cavity fed dipole array antenna using ENZ metamaterial for 5G applications," *Sensors*, Vol. 22, 1–12, 2022.
87. Alibakhshikenari, M., E. M. Ali, M. Soruri, M. Dalarsson, M. Naser-Moghadasi, B. S. Virdee, C. Stefanovic, A. Pietrenko-Dabrowska, S. Koziel, S. Szczepanski, and E. Limiti, "A comprehensive survey on antennas on-chip based on metamaterial, metasurface, and substrate integrated waveguide principles for millimeter-waves and terahertz integrated circuits and systems," *IEEE Access*, Vol. 10, 3668–3692, 2022.
88. Althuwayb, A. A., M. Alibakhshikenari, B. S. Virdee, H. Benetatos, F. Falcone, and E. Limiti, "Antenna on Chip (AOC) design using metasurface and SIW technologies for THz wireless applications," *Electronics*, Vol. 10, 1120, 2021.

89. Alibakhshikenari, M., B. S. Virdee, A. A. Althuwayb, D. Mariyanayagam, and E. Limiti, "Compact and low-profile on-chip antenna using underside electromagnetic coupling mechanism for terahertz front-end transceivers," *Electronics*, Vol. 10, 1264, 2021.
90. Alibakhshikenari, M., B. S. Virdee, C. H. See, R. Abd-Alhameed, F. Falcone, and E. Limiti, "A novel 0.3–0.31 THz GaAs-based transceiver with on-chip slotted metamaterial antenna based on SIW technology," *IEEE Asia-Pacific Microwave Conference*, 2019.
91. Alibakhshikenari, M., B. S. Virdee, A. A. Althuwayb, S. Aissa, C. H. See, R. Abd-Alhameed, F. Falcone, and E. Limiti, "Study on on-chip antenna design based on metamaterial-inspired and substrate-integrated waveguide properties for millimetre-wave and THz integrated-circuit applications," *Journal of Infrared, Millimeter, and Terahertz Waves*, Vol. 42, 17–28, 2021, (<https://creativecommons.org/licenses/by/4.0/>).
92. Loghmannia, P., M. Kamyab, M. R. Nikkah, and R. Rezaiesarlak, "Miniaturized low-cost phased-array antenna using SIW slot elements," *IEEE Antennas and Wireless Propagation Letters*, Vol. 11, 1434–1437, 2012.
93. Celenk, E. and N. T. Tokan, "Frequency scanning conformal sensor based on SIW metamaterial antenna," *IEEE Sensors Journal*, Vol. 21, 16015–16023, 2021.
94. Nitas, M., V. Salonikios, S. Raptis, and T. V. Yioultsis, "Design of fully planar cost-effective metamaterial-enhanced SIW antennas for 5G applications," *16th European International Conference on Antennas and Propagation*, 2022.
95. Nitas, M., M. T. Passia, and T. V. Yioultsis, "Fully planar slow-wave substrate integrated waveguide based on broadside-coupled complementary split ring resonators for mmwave and 5G components," *IET Microwaves, Antennas & Propagation*, Vol. 14, 1096–1107, 2020.
96. Dong, Y., V. Zhurbenko, K. Kaslis, J. M. Bjorstorp, and T. M. Johansen, "Wideband split-ring antenna arrays based on substrate integrated waveguide for Ka-band applications," *International Journal of Microwave and Wireless Technologies*, Vol. 14, 524–536, 2022.
97. Hu, B., T. Wu, Y. Cai, W. Zhang, and B. L. Zhang, "A novel metamaterial-based planar integrated Luneburg lens antenna with wide bandwidth and high gain," *IEEE Access*, Vol. 08, 4708–4713, 2020.
98. Feng, C., T. Shi, and L. Wang, "Novel broadband Bow-Tie antenna based on complementary splitting resonators enhanced substrate-integrated waveguide," *IEEE Access*, Vol. 07, 12397–12404, 2019.
99. Jin, C. and A. Alphones, "Leaky-wave radiation behavior from a double periodic composite right/left-handed substrate integrated waveguide," *IEEE Transactions on Antennas and Propagation*, Vol. 60, 1727–1735, 2012.